NAVAL POSTGRADUATE SCHOOL

MONTEREY, CALIFORNIA

THESIS

INTEGRATION OF LEDS AS AN ALTERNATIVE COMMUNICATION SYSTEM FOR CUBESATS

by

Wee Seng Loh

September 2022

Thesis Advisor: Wenschel D. Lan
Co-Advisor: Giovanni Minelli

THIS PAGE INTENTIONALLY LEFT BLANK

REPORT DOCUMENTATION PAGE			*Form Approved OMB No. 0704-0188*

1. AGENCY USE ONLY *(Leave blank)*	**2. REPORT DATE** September 2022	**3. REPORT TYPE AND DATES COVERED** Master's thesis

4. TITLE AND SUBTITLE INTEGRATION OF LEDS AS AN ALTERNATIVE COMMUNICATION SYSTEM FOR CUBESATS	**5. FUNDING NUMBERS**
6. AUTHOR(S) Wee Seng Loh	
7. PERFORMING ORGANIZATION NAME(S) AND ADDRESS(ES) Naval Postgraduate School Monterey, CA 93943-5000	**8. PERFORMING ORGANIZATION REPORT NUMBER**
9. SPONSORING / MONITORING AGENCY NAME(S) AND ADDRESS(ES) N/A	**10. SPONSORING / MONITORING AGENCY REPORT NUMBER**

11. SUPPLEMENTARY NOTES The views expressed in this thesis are those of the author and do not reflect the official policy or position of the Department of Defense or the U.S. Government.

12a. DISTRIBUTION / AVAILABILITY STATEMENT Approved for public release. Distribution is unlimited.	**12b. DISTRIBUTION CODE** A

13. ABSTRACT (maximum 200 words)

The recent reduction in launch costs coupled with lower development costs has lowered the barrier of entry for satellite development and deployment, resulting in increasing numbers of satellites launched for civil, commercial, and educational institutions in the past decade. CubeSats are often manifested as secondary payloads onboard launch vehicles and are often deployed into the same orbit over a short time period. It has become difficult or impossible to immediately distinguish and track a specific satellite with traditional tracking methods using their onboard radio frequency (RF) communication systems. This thesis focuses on using light emitting diodes (LED) installed on a CubeSat to achieve tracking of the CubeSat in low-earth orbit (LEO) shortly after deployment and to that then utilize the LED payload to transmit the operating status or operational data to the ground stations.

14. SUBJECT TERMS CubeSats, LEDs, communication, satellite	**15. NUMBER OF PAGES** 77
	16. PRICE CODE

17. SECURITY CLASSIFICATION OF REPORT	**18. SECURITY CLASSIFICATION OF THIS PAGE**	**19. SECURITY CLASSIFICATION OF ABSTRACT**	**20. LIMITATION OF ABSTRACT**
Unclassified	Unclassified	Unclassified	UU

NSN 7540-01-280-5500

Standard Form 298 (Rev. 2-89)
Prescribed by ANSI Std. 239-18

THIS PAGE INTENTIONALLY LEFT BLANK

Approved for public release. Distribution is unlimited.

INTEGRATION OF LEDS AS AN ALTERNATIVE COMMUNICATION SYSTEM FOR CUBESATS

Wee Seng Loh
Military Expert 5, Republic of Singapore Air Force
BEE, National University Of Singapore , 2012

Submitted in partial fulfillment of the
requirements for the degree of

MASTER OF SCIENCE IN SPACE SYSTEMS OPERATIONS

from the

NAVAL POSTGRADUATE SCHOOL
September 2022

Approved by: Wenschel D. Lan
Advisor

Giovanni Minelli
Co-Advisor

James H. Newman
Chair, Space Systems Academic Group

THIS PAGE INTENTIONALLY LEFT BLANK

ABSTRACT

The recent reduction in launch costs coupled with lower development costs has lowered the barrier of entry for satellite development and deployment, resulting in increasing numbers of satellites launched for civil, commercial, and educational institutions in the past decade. CubeSats are often manifested as secondary payloads onboard launch vehicles and are often deployed into the same orbit over a short time period. It has become difficult or impossible to immediately distinguish and track a specific satellite with traditional tracking methods using their onboard radio frequency (RF) communication systems. This thesis focuses on using light emitting diodes (LED) installed on a CubeSat to achieve tracking of the CubeSat in low-earth orbit (LEO) shortly after deployment and to that then utilize the LED payload to transmit the operating status or operational data to the ground stations.

THIS PAGE INTENTIONALLY LEFT BLANK

TABLE OF CONTENTS

LIST OF FIGURES

LIST OF TABLES

THIS PAGE INTENTIONALLY LEFT BLANK

LIST OF ACRONYMS AND ABBREVIATIONS

BJT	Bipolar junction transistor
CMOS	Complementary metal-oxide semiconductor
COTS	Commercial-off-the-shelf
CSpOC	Combined Space Operations Center
DOD	Depth of discharge
EM	Electro-magnetic
FPGA	Field programmable gate arrays
FVEY	Five Eyes
GPIO	General purpose input output
ISS	International Space Station
LED	Light emitting diode
LEO	Low Earth orbit
MODTRAN	MODerate resolution atmospheric TRANsmission
NASA	National Aeronautics and Space Administration
NIR	Near-Infrared
RF	Radio frequency
RGB	Red, green, blue
SLS	Space launch system
SSA	Space situational awareness
SSN	Space surveillance network
SSO	Sun synchronous orbit
TLE	Two-line elements
TRL	Technology readiness level
UART	Universal asynchronous receiver/transmitter
USB	Universal serial bus

THIS PAGE INTENTIONALLY LEFT BLANK

ACKNOWLEDGMENTS

First, I would like to take this opportunity to thank my advisors, Dr. Wenschel Lan and Dr. Giovanni Minelli, for their support, time and giving me guidance through my entire journey for this research. I would also like to thank Mr. Jim Horning who had provided invaluable guidance and assistance on programming. A special thanks dedicated to my teammates from AE4831 (Spacecraft System II); MAJ Edwin, MAJ Jun Jie, MAJ Giuliano and LT Katherine. Without their support, it would not be possible to perform the standoff distance testing with the telescope and payload outside of the NPS campus.

Last but not least, I would never achieve this master's degree without the support of my lovely wife, Fiona. I owe the biggest thanks to her and family for their encouragement and support during this period in NPS.

THIS PAGE INTENTIONALLY LEFT BLANK

I. INTRODUCTION

Since Sputnik 1 was launched in October 1957 by the Soviet Union, marking the first satellite in space, the number of satellites in orbit has grown steadily, particularly in the last decade. The number of active satellites in 2011 and 2021 were 1033 and 4877, respectively, which represents more than four times the number of satellites in a mere ten-year period [1], as depicted in Figure 1. Historically, nations such as the United States and the Soviet Union (Russia) have dominated the population of satellites in orbit since the Cold War period. Recently, emerging superpowers and many developed countries such as China and India are increasing their presence and effort in sending satellites into space. Figure 2 shows the breakdown of satellites in orbit as of April 2020. Tracking of satellites, especially for very small satellites such as CubeSats, has been increasingly challenging with the surge in low-Earth orbit (LEO) constellations. In one example, direct tracking of the swarm satellites developed by the European Space Agency (ESA) was lost more than 160 times during its first two years in orbit whenever there are ionospheric thunderstorms [2].

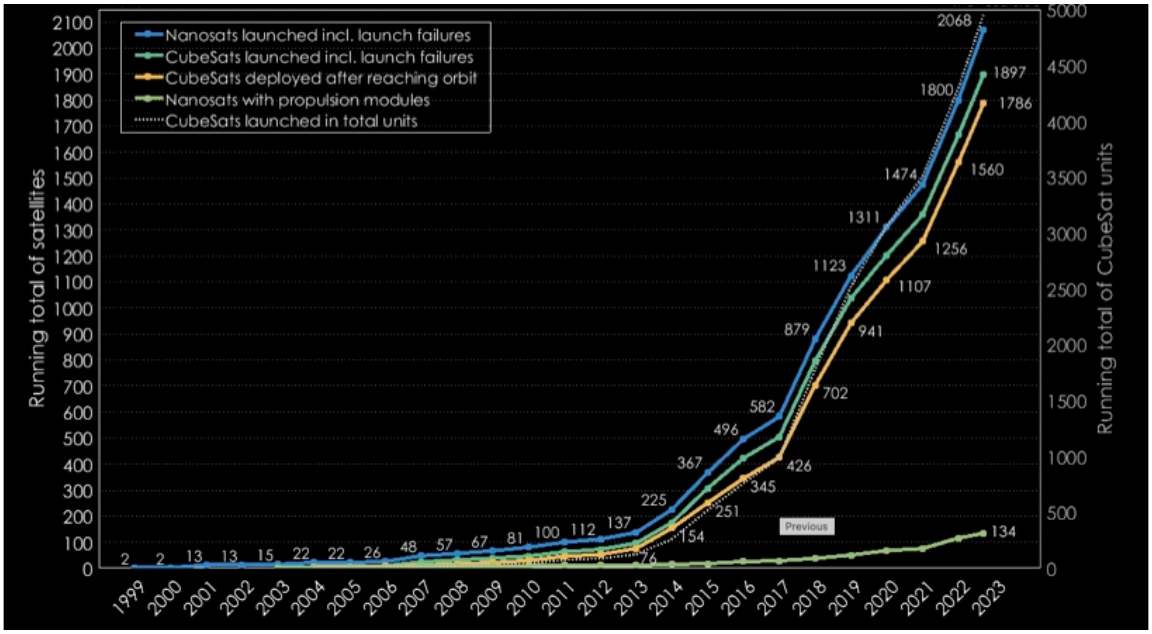

Figure 1. Number of active satellites between 1999 and 2022. Source: [3].

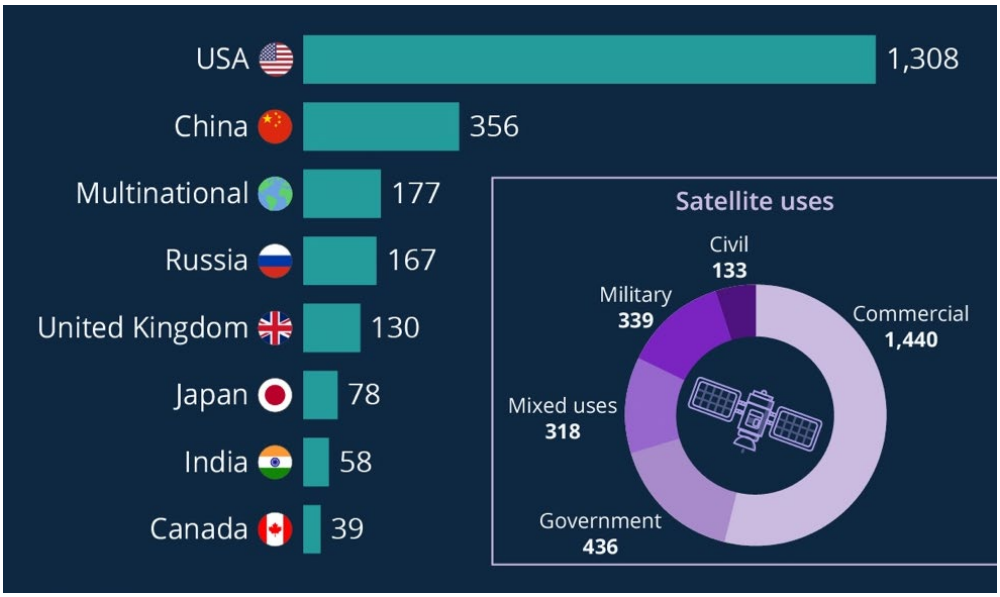

Figure 2. Satellites in orbit by country, as of April 2020. Adapted from [4].

A. CUBESAT

Very small satellites, also known as CubeSats, conform to standard dimension of a 10 cm cubed (10 cm x 10 cm x 10 cm) for each unit (Unit or U). CubeSats are commonly built in 1U, 1.5U, 2U, 3U, 6U, or 12U in size and weigh approximately 1.33 kg/U [5], as depicted in Figure 3. There are some variations in both weight and size based on the mission and/or the payloads they carry.

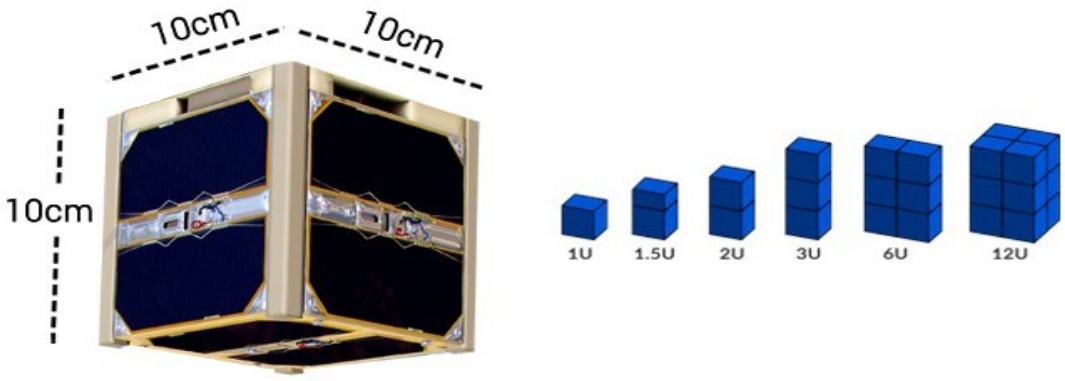

Figure 3. Standard dimensions of a CubeSat. Adapted from [6].

The CubeSat standard was first conceptualized in the late 1990s as a joint effort between two professors from California Polytechnic State University and Stanford University, to allow students to gain valuable engineering experience and knowledge in satellites [7]. In recent decades, the surge in CubeSats development has been primarily fueled by the low developmental cost and declining launch costs. As of June 2022, it is estimated that there are more than 3,500 CubeSats in orbit, and another 2,500 CubeSats are projected to be launched in the next six years [3].

Traditional satellite missions such as the Artemis and Psyche missions led by the National Aeronautics and Space Administration (NASA), which are scheduled for launch in 2022, would cost over $4 billion [8] and $850 million [9], respectively. In comparison, utilizing primarily commercial-off-the-shelf (COTS) components, fast development cycles, and increased tolerance for risk, the development cost and time required to build a CubeSat has substantially shrunk [10]. One study in 2016 estimated that the cost of a typical university-built CubeSat development ranged from $50,000 and $200,000 [11]. The low cost and quick development cycles, among many other advantages of CubeSats [12], have allowed space enthusiasts from academic institutions, private companies, and government organizations to pioneer, demonstrate capabilities, or gather data at a smaller scale before extending out to larger-scale missions.

In most space launches, the primary payload is a large, heavy, expensive spacecraft. CubeSats are installed as small secondary payloads, and they are released separately from the primary payload on the same flight to space. For instance, the Artemis I mission was equipped with ten CubeSats in the main rocket's stage adapter [13]. Figure 4 shows the installation of the CubeSats in the Space Launch System (SLS) rocket's stage adapter.

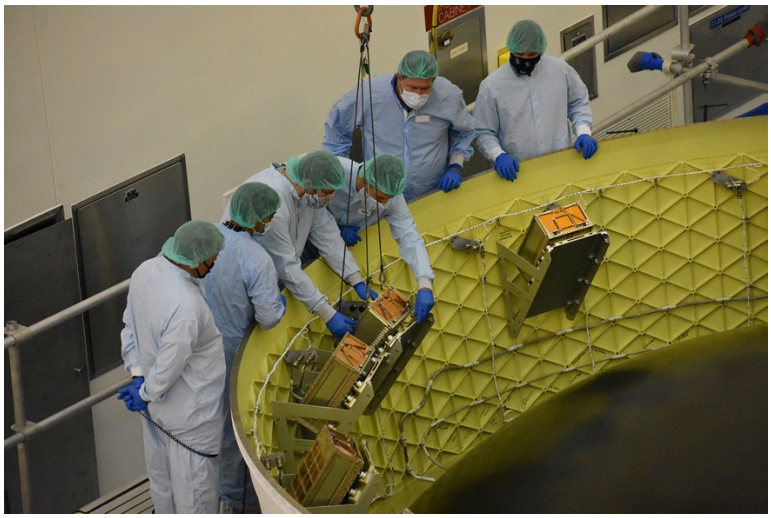

Figure 4. Installation of CubeSat in the rocket's stage adapter for Artemis I Mission. Source: [13].

The development of commercial launch systems has significantly reduced the cost of space launch since the 1950s, led by the development of reusable launch systems such as the Falcon 9. The cost to launch for every kilogram to LEO was over $100,000/kg in the 1950s and 1960s. While cost of launch continued to decline over the next few decades, it remained over $10,000/kg until the early 2000s. The development of Falcon 9 and Falcon Heavy have since reduced the cost of space launch to $2,700/kg and $1,400/kg [14], respectively, as depicted in Figure 5. As a result, the reduction in launch cost coupled with the low development cost has lowered the barrier of entry to space for CubeSats over the past decade.

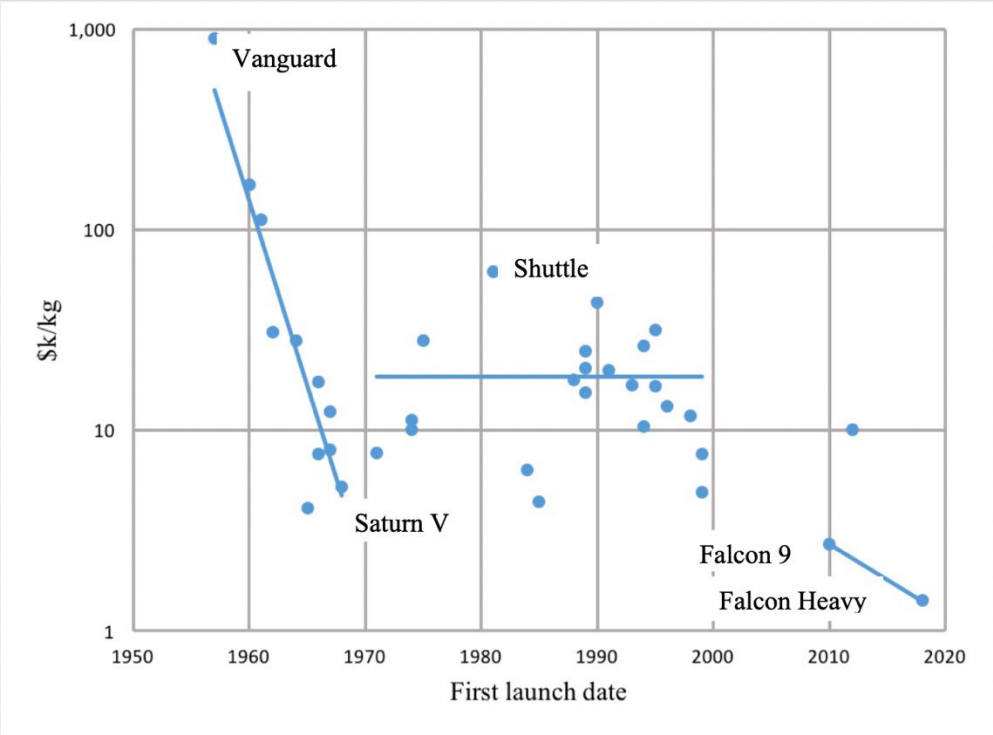

Figure 5. Launch cost per kilogram to LEO since first launch date. Source: [14].

Nonetheless, CubeSats are not without their disadvantages and challenges in both development and operation. CubeSats have a shorter lifespan as compared to traditional satellites as they have little or no propulsion to perform high delta-V maneuver or station keeping after they launch into LEO. Furthermore, the small size of the CubeSat as compared to larger satellite programs increases the challenge of tracking CubeSats. While ground stations such as the Mobile CubeSat Command and Control (MC3) network operated by the Naval Postgraduate School (NPS) can use the predicted coordinates and trajectory of the CubeSat, the task to identify a particular CubeSat becomes increasingly difficult as the number of CubeSats released from the launch vehicle increases.

B. TRADITIONAL TRACKING OF CUBESAT

Space Situational Awareness (SSA) is the process of tracking objects in orbit and predicting their location with the Two-Line Elements (TLE) for each tracked object [15]. The U.S. Space Surveillance Network (SSN) is equipped with a combination of optical and

radar sensors to support the Combined Space Operations Center's (CSpOC) mission to detect, track, identify, and catalog all manmade objects orbiting the Earth [16]. Ground-based radar has been the prevalent method the majority of satellite and space object since the first manmade satellite, Sputnik 1. Advancements in radar technology, such as the phased-array radars, have increased the throughput of each radar scan to allow multiple satellites to be tracked simultaneously.

In 2018, Spaceflight successfully launched its first dedicated ridesharing mission the sun synchronous orbit (SSO) with over 64 MicroSats and CubeSats from more than 30 different organizations or educational institutions. After the CubeSats were deployed into the same orbit over a short timeframe, identifying the position of a particular CubeSat was particularly difficult [17]. Thus, it became difficult or impossible to immediately distinguish and track a specific satellite with traditional tracking methods through their onboard radio frequency (RF) communication system. Instead, ground operators have to follow the orbital elements of the launch vehicle until better positions are determined, as the CubeSats will drift away after some time. Furthermore, the difficulty of tracking increases if there are multiple CubeSats that are not working, which consequently increases troubleshooting time. With more than 1,200 operational CubeSats in LEO [3], many CubeSats could take up to weeks or months before establishing positive contact with the ground station, while there are some that may never be identified, becoming space debris [18]. A related issue includes the management of the RF spectrum itself, which is becoming increasingly congested with more CubeSats in operation [19], and users trying to track the satellites may experience interference due to the congested RF bands.

C. OPTICAL TRACKING OF CUBESATS IN LEO

Optical tracking of satellites using COTS telescopes is an alternative tracking method to supplement the RF communication path and increase the chance of acquiring the CubeSat as early as possible. Nonetheless, it will only provide marginal improvement as optical tracking requires the satellite to be in the sunlight while the ground telescope is in darkness. This requirement constraints the optical tracking activity to periods of twilight. As discussed earlier, CubeSats are usually launched into space as secondary payloads,

limiting the user's control over the number of CubeSats at each launch and the time of release. Therefore, optical tracking yields limited improvement or benefits to tracking the CubeSat. Active illumination aids such as light-emitting diodes (LED) installed on the CubeSat's exterior surface, on the other hand, could improve tracking and acquisition of CubeSat as early as the deployment from the launch vehicle. With active onboard illumination, ground stations can track the CubeSat at night, and this can reduce the time required for identification. LEDs on the CubeSat can also perform a secondary function, serving as a backup or secondary data downlink when the primary radio communication system fails [15]. This LED communication system could transmit information such as the CubeSat's operating status or a fault message. In addition, the LED system, which requires less power than most radio communication system, can continue to provide critical information and allow tracking of the CubeSat toward the end of the satellite's life when the solar panels deteriorate and the battery does not generate sufficient power for all the sub-systems.

D. THESIS OVERVIEW

This thesis focuses on using light emitting diodes (LEDs) installed on the CubeSat to achieve tracking of a CubeSat in LEO, and to utilize the LED payload to transmit the operating status or operational data to the ground stations. A fundamental knowledge of electromagnetic (EM) spectrum and link budget analysis forms the foundation of the system design described in Chapter II. Chapter III addresses the methods and desired results to validate the LED payload and link budget. The results from the link budget measurement are analyzed and discussed in Chapter IV. Finally, conclusions and recommendations for future study are highlighted in Chapter V.

THIS PAGE INTENTIONALLY LEFT BLANK

II. ELECTROMAGNETIC SPECTRUM FUNDAMENTALS AND DESIGN CONSIDERATIONS

This chapter discusses electromagnetic (EM) spectrum concepts relevant to this research and how the Earth's atmosphere can attenuate the transmitted power from an LED. This information subsequently contributes to the selection criteria for the LED type. The chapter concludes with a power and thermal analysis that guide the selection criteria for the other components of the payload.

A. ELECTROMAGNETIC SPECTRUM AND OUR ATMOSPHERE

Understanding the EM spectrum and how different environmental conditions can affect the transmissibility of light propagation is critical for this research. The EM spectrum can be represented in frequency or wavelength as shown in Equation (1), spreading from the radio frequency in the kilohertz range to gamma rays in the terahertz range. Figure 6 depicts the EM spectrum and the typical applications associated with each area of the spectrum.

$$\lambda = \frac{c^1}{f\ (Hz)} \tag{1}$$

The Sun in our solar system is considered the closest approximation to a perfect black body object. A black body object absorbs light across all wavelengths without any reflection and emits energy across the entire EM spectrum. The temperature of the Sun's surface is approximately 6,000 K (5,727° C), which is where most of the EM radiation is emitted across the visible wavelength region [19]. Our atmosphere forms a protective layer by reflecting and absorbing most of the higher energy wavelengths from reaching the Earth's surface. As shown in Figure 6, only EM radiation in the visible light and radio frequency regions can penetrate our atmosphere. The focus of this thesis is only on the visible light region between 400 nm (400 x 10^{-9} m) and 700 nm (700 x 10^{-9} m), and the

[1] c is the speed of light in vacuum, c = 2.998 x 10^8 m/s

subsequent sections of this chapter discuss how light signal attenuation is accounted for in the optical link budget equation.

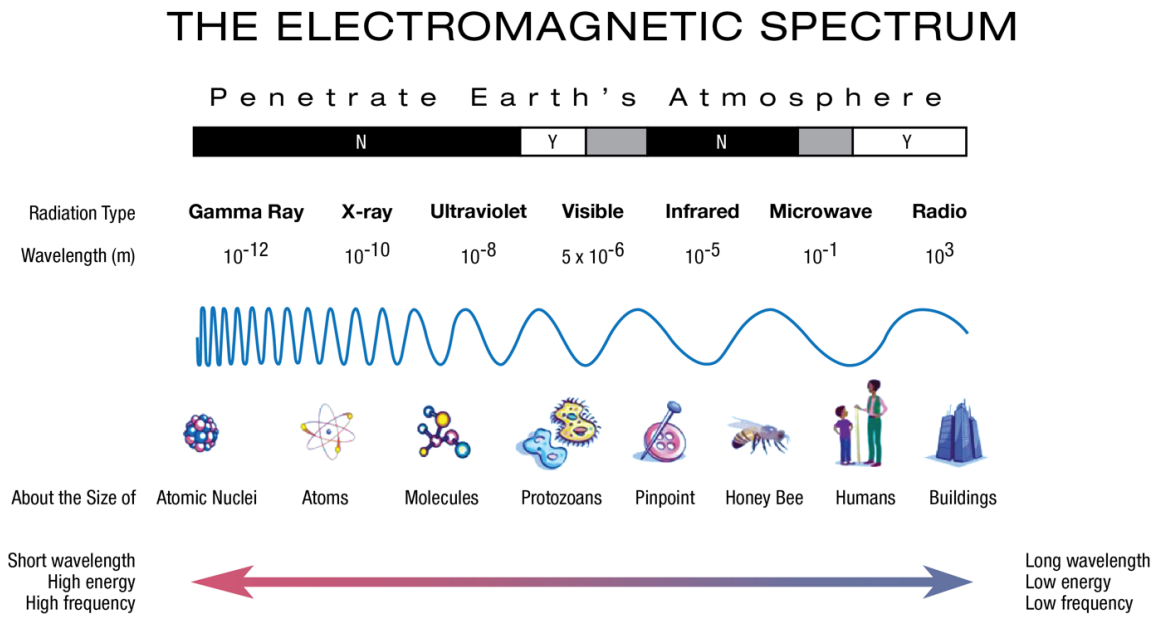

Figure 6. Electromagnetic spectrum. Source: [21].

B. OPTICAL LINK BUDGET

The optical link budget, or link budget, is a quantitative indication of the total amount of gain and loss between the transmitter and receiver for successful communication. For any successful communication system, the link budget provides a quantitative estimate if there is sufficient received power so the message can be decoded by the ground station. Equation (2) depicts the link budget, where P_T is the power of the transmitter, P_R is the received power, and L_a, L_e, and L_{geom} are the atmospheric, extinction, and geometric losses, respectively [22]. Due to the long distance between the satellite and ground terminal, geometric and extinction losses will be the most prominent losses in the link budget calculation. The link margin analysis in [22] is based on terrestrial free-space communication with geometric loss being the main contributor followed by the atmospheric extinction loss and atmospheric turbulence loss. Leveraging terrestrial free-

space communication provides the most conservative result when modeling the atmospheric extinction loss given the density of the atmosphere at sea level.

$$Link\ Margin\ (dB) = P_T - (P_R + G_R + L_a + L_e + L_{Geom}) \quad (2)$$

1. Atmospheric Extinction Loss (Le)

Depending on the wavelength, an optical wave will experience attenuation of its energy as it travels through the atmosphere, which is made up of aerosols, dust, water droplets, and many other particles. The two main effects that result in the attenuation of the signal strength are scattering and absorption.

Scattering refers to the redirection of optical waves when they come into contact with suspended particles in the atmosphere. There are three main types of scattering effects, namely, Rayleigh, Mie, and geometrical. The key difference between them is due to the scattering effects from different particle size and the wavelength of the optical wave [23]. Rayleigh scattering occurs when the scattering particle radius is much smaller than the optical light's wavelength. Mie scattering occurs when the radius of the scattering particles is slightly larger than wavelength. Lastly, geometric scattering occurs at a larger particle radius to wavelength ratio, as in the case of rain, snow, and thick fog. Rayleigh scattering is the main contributor to the "blue" and "red" sky during daytime and sunset or sunrise. Due to the shorter wavelength of the blue light, it scatters in all directions, causing the sky to look blue during the day. During sunset, sunlight needs to travel further as the sun is closer to the horizon which causes more blue light to be scattered or removed, leaving mostly red light; thus, the red sky during sunset or sunrise.

Absorption occurs when the energy of the photons from the optical waves is transformed to thermal energy when it interacts with atmospheric particles such as water, oxygen, carbon dioxide, and ozone [23]. Figure 7 depicts the atmospheric absorption through the atmosphere. It can be observed that apart from the radio frequency, the visible light range has a relatively lower atmospheric attenuation across the entire EM spectrum.

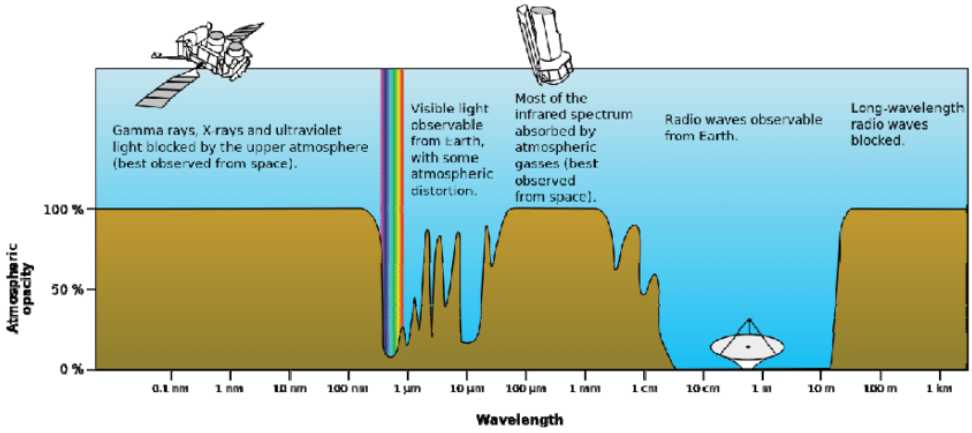

Figure 7. Atmospheric absorption across the EM spectrum. Source: [24].

The extinction coefficient is a combination of absorption (α) and scattering (β) by particles in the atmosphere [25], which can be represented by Beer-Lambert's law, as shown in Equation (3). The extinction loss (L_e) is expressed by the extinction coefficient ($\alpha_e(\lambda)$) and the atmospheric path distance (d).

$$L_e(dB) = -10\, log_{10}[e^{-\alpha_e(\lambda)d}] \tag{3}$$

The extinction coefficient is also known as the atmospheric attenuation coefficient, which describes the extinction level of the medium and is expressed in terms of its meteorological visibility, V, which is defined as the distance at which transmittance will fall to 2% from the original value [22]. It is modeled with the Kruse formula in Equation (4), where V is the visibility in meters, δ is the particle size distribution coefficient and λ is wavelength in nanometer. Figures 8 and 9 show the visibility and particle size distribution in different weather conditions, respectively.

$$\alpha_e(\lambda) = \frac{3.91}{V}\left(\frac{\lambda}{550}\right)^{-\delta} \tag{4}$$

Weather condition	Visibility range, V (km)
Thick fog	0.2
Moderate fog	0.5
Light fog	0.770–1.0
Thin fog/heavy rain (25 mm/h)	1.9–2.0
Haze/medium rain (12.5 mm/h)	2.8–40.0
Clear/drizzle (0.25 mm/h)	18.0–20.0
Very clear	23.0–50.0

Figure 8. Weather conditions and their visibility range. Source: [22].

$$\delta = \begin{cases} 1.6 \text{ for } V > 50 \text{ km} \\ 1.3 \text{ for } 6 \text{ km} < V < 50 \text{ km} \\ 0.585\, V^{1/3} \text{ for } V < 6 \text{ km} \end{cases}$$

Figure 9. Particle size distribution coefficient. Source: [22].

The atmospheric extinction loss model presented in [22] is based on terrestrial free-space communications and it does not factor the decreasing atmospheric density as altitude increases. According to the MODTRAN (MODerate resolution atmospheric TRANsmission) model, the atmospheric profiles in Figure 10 show that the H_20 and O_3 composition will decrease to less than $1–^8$ atm at 100 km [26]. Separate research performed a comparison of the air density between the MODTRAN model with actual measurements (Figure 11) further confirming that the atmospheric density is minimal beyond 40 km [27]. Therefore, creating a practical limit of 100 km, also known as the Kármán line, creates significant design margin for losses due to atmospheric extinction losses from absorption and scattering given Equation 3's assumption of uniform sea-level atmospheric density.

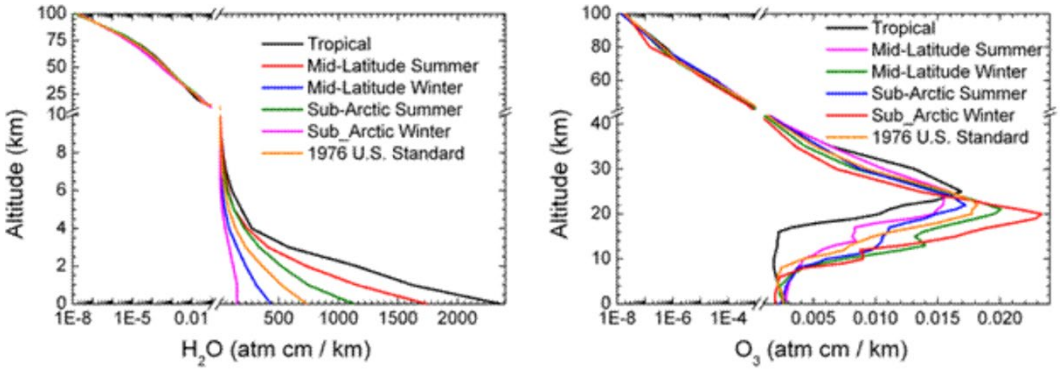

Figure 10. MODTRAN model of atmospheric profiles for H20 and O3 up to 100 km altitude. Source: [26].

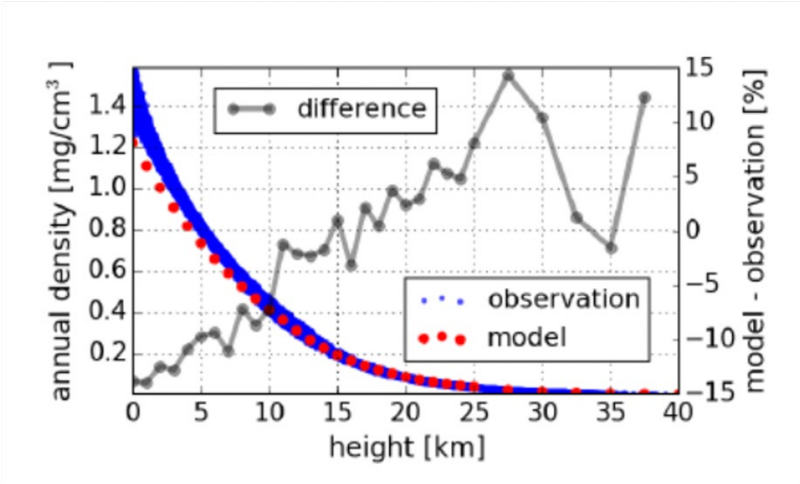

Figure 11. Comparison of atmospheric density between MODTRAN model and observation. Source: [27].

2. Geometric Loss

Light propagates in the form of photons, and as it travels through space, the optical wave will diverge and the remaining photons that reach the receiver's aperture will be of lower magnitude as compared to that at the transmitter end. This divergence of the optical beam is known as geometric loss. Figure 12 shows the effect of beam divergence as it travels from the transmitter to the receiver plane. It can be represented mathematically by the ratio of the receiver aperture area to the beam area at the receiver plane as shown in Equation (5) [22].

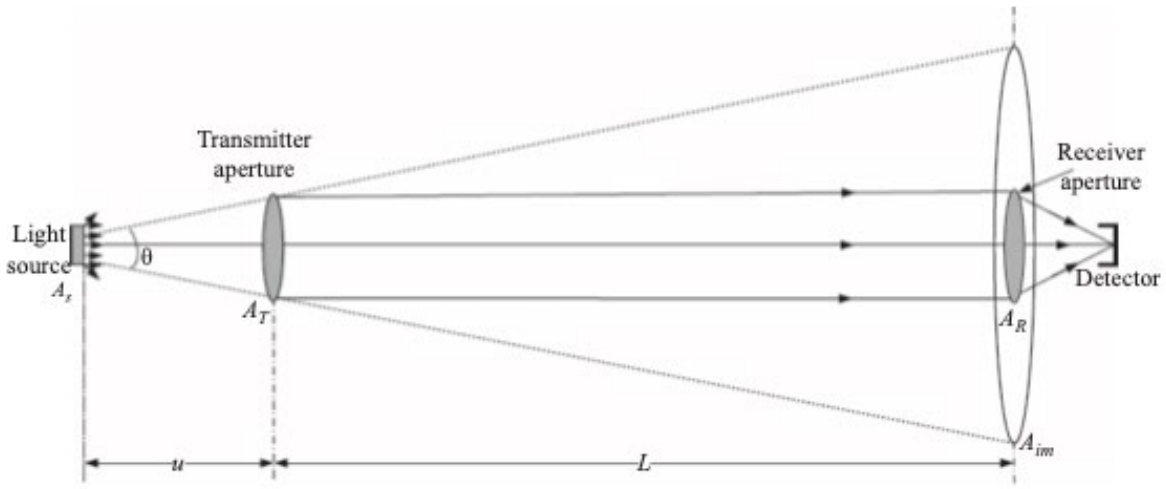

Figure 12. Geometric loss. Source: [22].

$$L_{Geom} = -10log\frac{A_R}{A_B} = -20\,log[\frac{D_R}{D_T+\theta*L}] \quad (5)$$

where

A_R is the area of the receiver aperture;

A_B is the area of the beam at the receiver plane;

D_R is the diameter of the receiving aperture in meters (m);

D_T is the diameter of the transmitting aperture in meters (m);

L is the link distance in kilometer (km); and

θ is the divergence angle of the beam in milli-radians [22].

3. Atmospheric Turbulence / Scintillation

When the Sun's energy is absorbed by the Earth and heats up the surface, the warm air will rise and mix with the cooler air at higher altitudes. This causes a fluctuation of atmospheric temperature and pressure in the atmosphere, resulting in pockets of atmosphere with differing temperatures [22]. This effect is known as scintillation, which would affect the optical wave transmitted over a long distance, and it can be modeled with Andrew's method as shown in Equation (6). However, it is difficult to identify or model the atmospheric turbulence for a specific time or location. Figure 13 depicts the magnitude of losses across different distances with a visibility range of 2 km showing that scintillation

is the minimal contributor to the overall losses. Therefore, the atmospheric loss (L_a) is not considered for the rest of this thesis.

$$L_a(dB) = 10\,log\,\sqrt{1 - \bar{\sigma}_I^2(D_R)} \tag{6}$$

Link distance L (m)	L_{Geom} (dB)	L_e (dB)	L_a (dB)
1,000	22.1102	3.9563	0.2634
1,500	25.5751	5.9344	0.4986
2,000	28.0452	7.9125	0.7900
2,500	29.9662	9.8907	1.0782
3,000	31.5383	11.8688	1.1494
3,500	32.8691	13.8469	0.8492
4,000	34.0227	15.8251	0.4344

Figure 13. Magnitude of losses across different distances, with visibility range of 2 km. Source: [22].

C. LED OPERATING WAVELENGTH

The atmospheric extinction loss is the only term in the link budget equation that is dependent on the wavelength, and it is the main contributor in the link budget analysis. Therefore, the LED's operating wavelength will have significant impact to the overall performance of the LED communication system and increase the chance of closing the optical link between the CubeSat and ground terminal. Figure 14 shows wavelengths and colors of the visible light range.

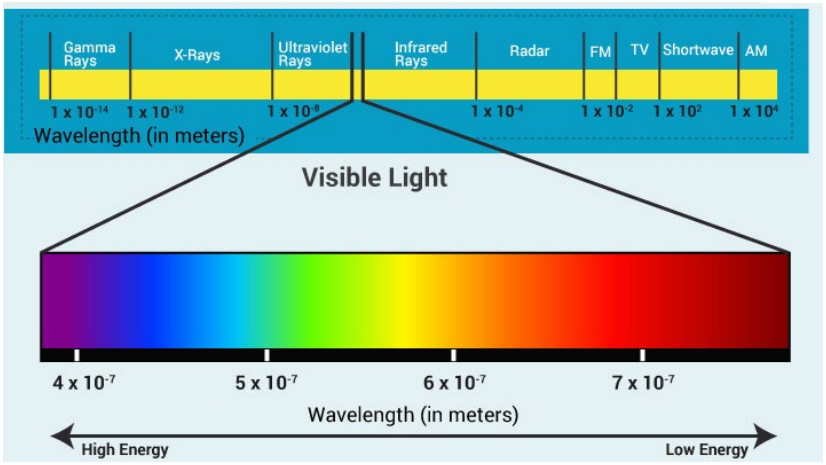

Figure 14. Visible light spectrum. Source: [28].

Using commercially available LED components, we studied the commonly available LEDs at the following wavelengths: 430 nm (blue), 550 nm (green), and 680 nm (red). Using the mathematical model in the earlier section, we can calculate the amount of atmospheric extinction loss from Equation (3) at a particular wavelength given that the attenuation increases with decreasing wavelength. Based on clear weather conditions and a transmission distance of 100 km, the respective atmospheric extinction losses for these LEDs are shown in Table 1, showing that the atmospheric extinction loss decreases as the wavelength increases based on Equation (3).

Table 1. Atmospheric extinction loss in very clear weather conditions (Visibility = 50 km).

	Blue	Green	Red
Wavelength (nm)	430	550	680
Visibility (km)	50	50	50
Particle Size Distribution	1.6	1.6	1.6
Atmospheric Extinction Loss, L_e (dB)	50.4	36.0	16.9

While theory provides a good approximation of the transmissibility of light through the atmosphere, it does not consider the effects caused by the different refractive indices from the different elements in the atmosphere. This can be supplemented with an established model such as the MODTRAN which computes the atmospheric spectral

transmittance. Figure 15 shows the transmittance percentage across the visible light spectrum. Comparing the transmittance across the three LED wavelengths (blue: 430 nm, green: 550 nm and red: 680 nm), it is determined that the green colored LED should provide the most consistent output.

While the Near-InfraRed (NIR) region between 700 nm and 900 nm yields higher transmittance and experiences lower extinction loss than the visible light ranges from 400 nm to 700 nm, it would be challenging for ground validation without using special equipment to validate the optical tracking of the CubeSat. Additional equipment such as a camera fitted with a filter is needed to see the NIR wavelength as the human eye is not capable of seeing wavelengths above 700 nm, making ground verification and testing difficult. Therefore, the NIR region is not considered in this thesis.

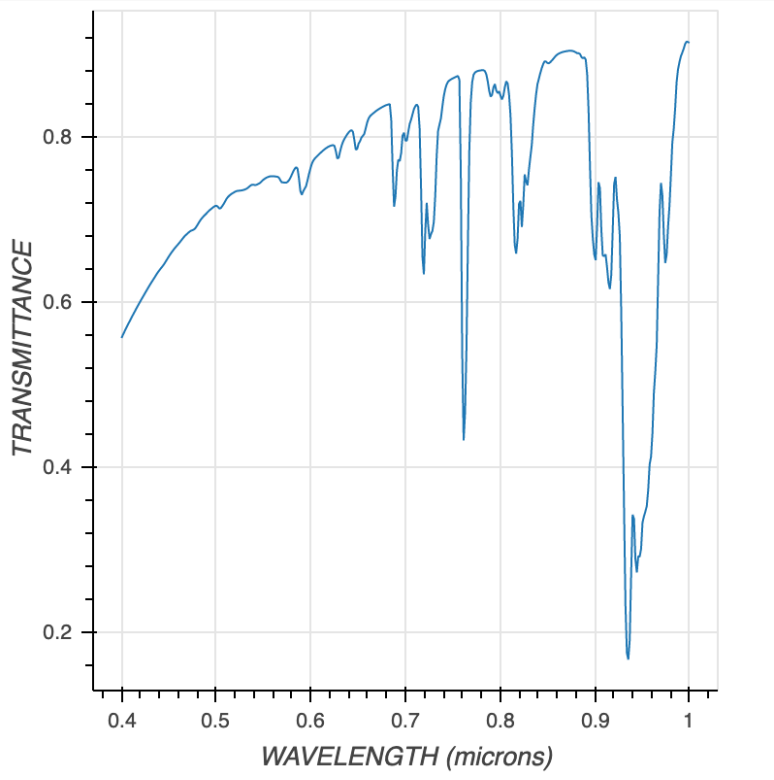

Figure 15. Transmittance percentage across visible light spectrum. Source: [26].

D. CUBESAT DESCRIPTION

The Space System Academic Group (SSAG) at NPS is currently developing two 6U CubeSats, Mola and Otter. The Mola and Otter CubeSats aim to boost the technology readiness level (TRL) of several technologies to benefit the Five Eyes (FVEY) small satellite development efforts and conduct experiments that are scalable. Both Mola and Otter CubeSat are built with the Astro Digital Corvus-6 bus, and the subsequent analysis in this thesis is conducted using the spacecraft configuration designed for the Mola CubeSat. However, the LED communication system is being considered as a candidate payload for Otter for the purposes of this effort.

This thesis will attempt to demonstrate an alternative communication system to the traditional RF communication system used for CubeSats. Leveraging the in-house environmental test and qualification facility at NPS, our objective was to design and develop a low-cost LED communication payload using easily accessible COTS components and software such as the Raspberry Pi. The Mola CubeSat uses the Astro Digital Corvus-6 bus, which offers approximately 0.5U of physical space for the LED communication system. Besides its primary mission to improve CubeSat tracking, the LED communication system can be an alternative communication payload for the CubeSat when the radio communication system is not operable.

E. ELECTRICAL POWER ANALYSIS

The small size of a CubeSat limits the number of batteries and solar arrays that it carries. Thus, electrical power analysis is important as it will determine the amount of power and duty cycle required for operating the LED payload in eclipse. Table 2 shows the list of sub-systems and the power draw from the CubeSat over one orbit during normal operation. The CubeSat takes approximately 95 mins to complete an orbit. To extend the longevity of the battery, the depth of discharge (DOD) for a lithium-ion battery should not exceed 60% [30]. This will provide over 10,000 charge/discharge cycles, which translates to slightly more than two years in orbit. Therefore, the maximum average energy that the LED payload can consume in each orbit needs to be under 10.7 W. The power

consumptions for each sub-system are of estimated value based on its initial design and the calculated data in Table 2 is only used for preliminary estimation of the power requirement.

Table 2. Mola's CubeSat power requirements.

Subsystems	**Duty Cycle per orbit (%)**	**Peak Power (W)**	**Average Power (W)**	**Average Energy (W)**
C&DH	100.0	3.0	3.0	4.8
GPS Receiver	100.0	1.3	1.3	2.1
Attitude Determination	100.0	1.9	1.9	3.0
Attitude Control	50.0	1.1	0.6	0.9
TT&C (Transmit)	30.0	10.0	3.0	4.8
TT&C (Receive)	70.0	0.2	0.1	0.2
Imaging Payload	25.0	7.5	1.9	3.0
Comms Payload 1	25.0	32.0	8.0	12.7
Total:		**49.3**	**19.8**	**31.3**

F. THERMAL ANALYSIS

Thermal analysis has a direct impact on the survivability of any component or system on the CubeSat as the CubeSat undergoes a wide range of temperature variations during its orbit. As CubeSats are launched as secondary payloads into orbit, aerodynamic heating is negligible for a satellite in a stable low earth orbit, simplifying the thermal analysis. Equations (7) and (8) depict the thermal equation for calculating the heat energy due to environment and temperature equilibrium for hot and cold cases, respectively [27].

$$Q_{env} = \alpha S\left[A_p + RA_R\right] + \varepsilon IRA_{IR} \quad (7)$$

$$T\ (deg\ C) = \sqrt[4]{\frac{Q_{env}+Q_{in}}{Q_{constant}}} - 273K \quad (8)$$

where

α is the absorptivity (unitless, 0 to 1);

S is the solar irradiance/constant (W/m^2);

A_P is the projected area towards the sun (m^2);

R is the Earth albedo coefficient (W/m^2);

A_R is the percentage of solar irradiance diffusely reflected from the earth (m^2);
ε is the emissivity (unitless, 0 to 1);
IR is the irradiance of IR energy from the earth (W/m^2); and
A_{IR} is the percentage normal to the heat-transfer direction (m^2) [30].

The solar heat flux (S), earth albedo coefficient (R), and the IR irradiance from earth (IR) are determined if the CubeSat is facing the Sun directly or if it is in eclipse (i.e., in the Earth's shadow). Table 3 lists the respective coefficients for both the hot and cold cases, and the calculated temperature for both scenarios. This calculated temperature for both hot and cold cases shall provide an approximation of the operating temperature range of the CubeSat, as the result varies with different surface materials or subsystems in the CubeSat. The calculated hot and cold scenarios suggest that the operating temperature range of the Mola CubeSat is from -9.5 to 44.9 deg C and this will influence the selection criteria of the components for the LED communication payload.

Table 3. Thermal coefficient for hot and cold conditions [30].

	Solar Heat Flux (W/m^2)	Earth Albedo Coefficient (W/m^2)	IR irradiance from Earth (W/m^2)	Temperature (deg C)
Hot Case	1419.0	19.7	224.4	**44.9**
Cold Case	1317.0	15.2	186.5	**-9.5**

THIS PAGE INTENTIONALLY LEFT BLANK

III. SYSTEM DESIGN AND VALIDATION METHOD

A. MODE OF OPERATION AND SYSTEM REQUIREMENTS

The LED communication payload will only operate over compatible ground stations at night for two main reasons: (1) required direct line-of-sight between the CubeSat and ground station, and (2) light energy from the Sun will significantly reduce the ability to track the LED payload during the day. Figure 16 provides a graphical representation of the actual operation. Besides its primary mission to improve CubeSat tracking, the LED communication system can be an alternative communication payload for the CubeSat when the radio communication system is not operable. Other requirements that would drive the development of this payload are as follows:

- Achieve the minimal link budget based on both calculated values and ground trials.
- Detect abnormal operating temperatures using both the Raspberry Pi internal CPU sensor and an external temperature sensor.
- Achieve a minimum data rate of 1 Mbps during ground validation for a message transmitted from the payload.
- Withstand a LEO thermal environment between -9.5 deg C to 44.9 deg C.
- Minimize payload size and interface requirements to maintain flexibility among satellite platforms

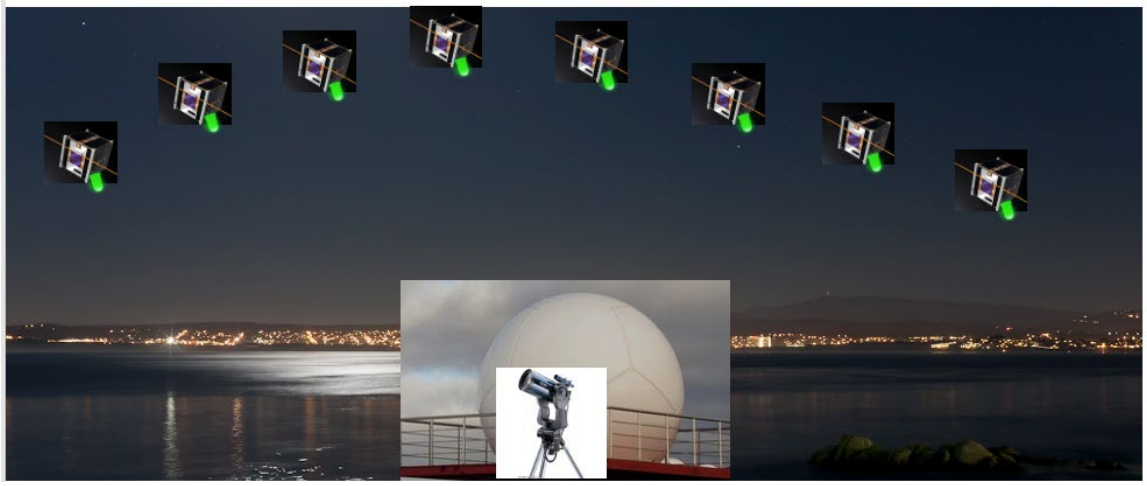

Figure 16. LED communication system operational concept

B. LED COMMUNICATION PAYLOAD DESIGN

1. Hardware Design

As discussed in Chapter II, the green colored LED operating approximately in the 530 nm wavelength region will yield the most optimal results and is readily available. Besides the LED wavelength, the power available on the CubeSat will also influence the LED selection. The Corvus-6 bus can supply 5 V and 8 V of electrical power to the payload. The Cree XP-E2 LED (P/N: XPEGRN-L1-0000-00D01) is selected as it has been used before by other research institutes for similar optical research [31], hence reducing the project risk. The Cree XP-E2 LED is designed to operate at 0.35 A with a forward voltage of 3.3 V. The TLC59213X LED driver is selected for this research as it can supply large output source currents up to 350 mA for eight LEDs. Figure 17 shows the prototype LED communication payload.

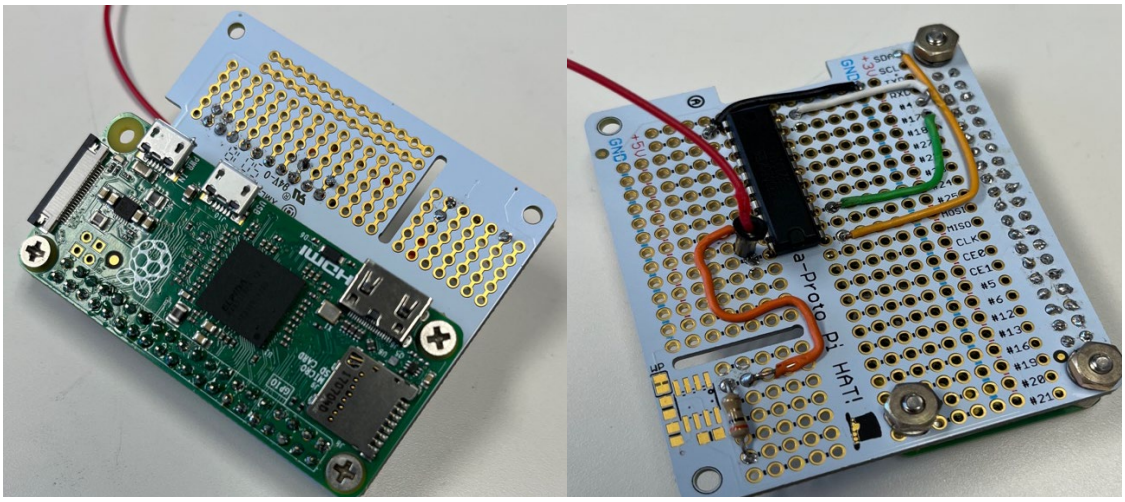

Figure 17. Prototype LED communication payload

2. Processor Selection

To achieve the objective for the system to be flexible and require only minimal modification or configuration changes for adaptation into future CubeSat designs which may not use the Corvus-6 bus, the payload is designed to have its own processing module. To ensure ease for future modification and achieve a low-cost solution, COTS components are leveraged where possible due to a large user base and ample examples available online. A comparison of microcontrollers (Arduino), microprocessors (Raspberry Pi), and field programmable gate arrays (FPGA) was done prior to final selection, as depicted in Table 4.

While all three types of processors are capable of meeting the requirement for the payload, it is the Raspberry Pi that was chosen as the most ideal for multiple reasons. There are peripheral ports such as ethernet and Universal Serial Bus (USB) ports, which could be used for communication between the CubeSat's main bus and the payload. Furthermore, the Raspberry Pi has a large user base to provide many examples, and several libraries are available in the outsource forum to use. In addition, the Raspberry Pi has internal temperature monitoring that can be read out directly and reduce the need for additional components for temperature monitoring and sensing. The Raspberry Pi is commonly used for many projects at NPS, and technical support is easily available within the NPS community as compared to another type of processor. Lastly, the Python programming

language is used more widely as compared to C / C++, and this will make any future modification easier on the Raspberry Pi. One main drawback with the Raspberry Pi, however, is its size as compared to the other processor types, but this can be overcome with the smaller sized Raspberry Pi Zero. One tradeoff with using the Raspberry Pi Zero is that it does not have an ethernet port; thus, communication between the CubeSat's main bus and the payload can only be achieved with the UART communication protocol.

Table 4. Comparison of microcontroller, microprocessor, and FPGA.

	Microcontroller (Arduino Uno)	**Microprocessor (Raspberry Pi 3B)**	**FPGA (Xilinx Spartan-3E)**
Processing Power	Low	High	Highest
Operating OS	Arduino Software (IDE)	Raspberry Pi OS (Linux-based)	Nil
Peripheral Ports	Requires add-on boards	USB, Ethernet, Wi-Fi, HDMI	Nil
Programming Language	C++	Python	C and C++
Field Reprogrammable	No	Yes	Yes
Size	6.9 cm x 5.3 cm (2.7 in x 2.1 in)	8.6 cm x 5.7 cm (3.37 in x 2.22 in)	2 cm x 2 cm
Cost	~$20	~$100	~$30

The data flow between the CubeSat and the LED payload is shown in Figure 18. The CubeSat status and messages will be communicated through the UART protocols to the Raspberry Pi of the LED payload represented by the red dotted box. The Raspberry Pi will control the LEDs by the LED driver with the input control signal (D1-D8) and output to the respective LEDs (Y1–Y8). The clock (CLK) and clear (CLR) are input latches to trigger and clear the outputs, respectively.

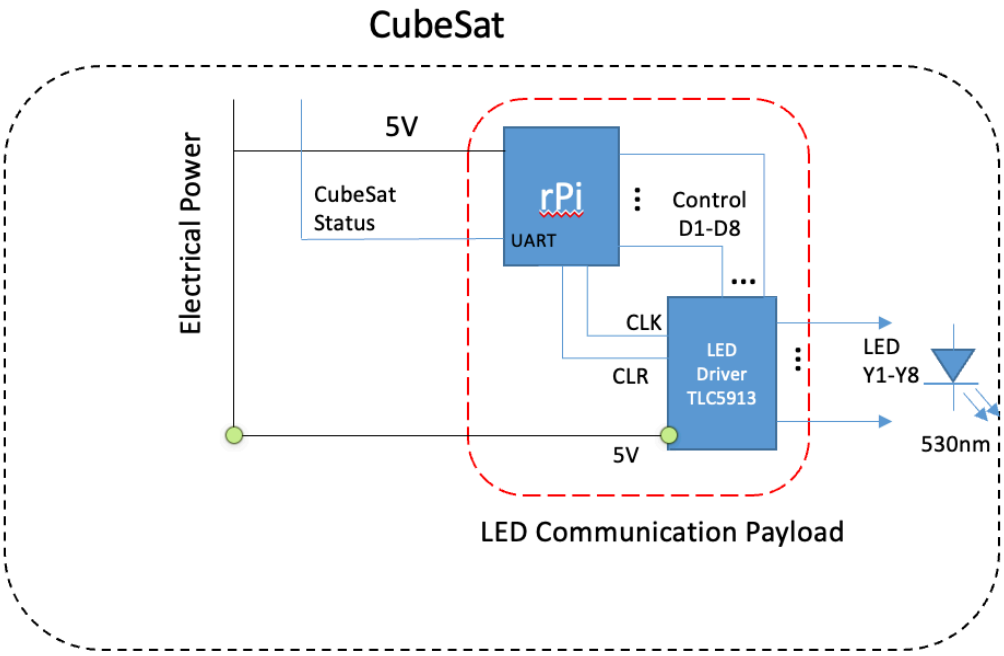

Figure 18. Data flow between CubeSat and LED communication system

C. LINK BUDGET AND DATA RATE VERIFICATION

Optical link budget analysis is critical in the final design of the LED communication system before any meaningful function such as performing optical tracking or optical communication between the CubeSat and ground station can be established. Without a link between the CubeSat and ground station, the system will be meaningless on the CubeSat. The methodology for validating the link budget and data rate measurement will be explained in this section.

1. Data Rate Verification and Analysis

The photoresistor, photodiode, and phototransistor are common electronic components that are available to sense light intensity and produce an electrical signal. The photoresistor is a basic component whose resistance value changes with respect to the amount of light it detects. However, the photoresistor has the slowest response time as compared to a photodiode or phototransistor, making it unsuitable for high data rates. Furthermore, the photoresistor's resistance value fluctuates as a function of temperature, making its output in this application unreliable. A photodiode behaves like a P-N junction

diode generating electric current when photons (light) hit the anode (light sensor area), creating electron-hole pairs that flow in the opposite directions towards the anode and cathode [32]. A phototransistor is similar to the photodiode except that it functions like a bipolar junction transistor (BJT) instead of a diode. A BJT comprised of an emitter, collector, and base terminal. The base terminal of a phototransistor is the light detector where the electrical current will be generated when photons hit the detector. The amount of current flowing between the emitter and collector terminal is determined by the number of photons received at the base terminal [33]. These components are ideal only for laboratory measurements or short distance (less than 1 m), due to the small surface area for light collection, as shown in Figure 19. While both the photodiode and phototransistor are feasible selections for this research, phototransistor requires additional amplification circuity. Therefore, the photodiode is used for the experiment and demonstration of the data rate of the LED communication payload given its simpler setup. Figure 20 shows the photodiode circuit designed for this research.

Figure 19. OSRAM Phototransistor, SFH 3310. Source: [34].

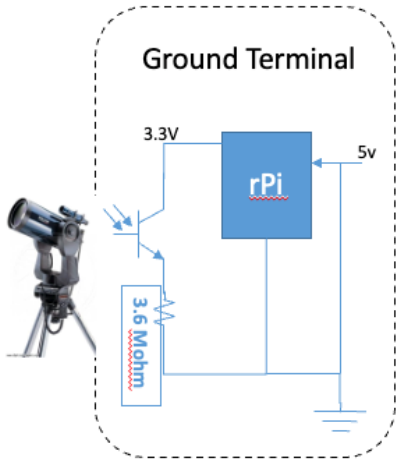

Figure 20. Photodiode circuit design

2. Link Budget Verification and Analysis

The link budget measurement is measured in outdoor setups, and the results are extrapolated up to 500 km to validate whether the optical link can be closed. This section examines the link budget verification method and its setup.

Ongoing research performing optical tracking of large satellites such as the International Space Station (ISS) using the MEADE 7-inch. LX200GPS Maksutov-Cassegrain telescope, a Canon Rebel T3i camera attached, generates an image that is processed for the intensity of light source. The Canon Rebel T3i uses a CMOS sensor with approximately 18 megapixels and is capable of recording up to 60 frames per second (fps) at 1,280 x 720 pixels. The camera is highly sensitive to visible light wavelengths, and post processing of images can indicate the intensity of the light signal, which can be translated to the power received. A pixel is the smallest element of a digital image and is represented in a two-dimensional grid (m x n pixels) [35]. Pixel intensity represents the number of light photons received, and can be represented in one value for a gray scale photo and three values (RGB) for a color photo [36]. In an 8-bit image, the pixel value ranges between 0 and 255, corresponding to the intensity or brightness at the particular pixel on the image [37], where 0 represents pitch dark and 255 representing the full-scale brightness that a camera can capture. Figure 21 displays images captured of the test setup for the telescope and LED payload.

Figure 21. Test setup from telescope and LED payload.

To validate the mathematical model of a link budget for atmospheric extinction loss (L_e) and geometric loss (L_{geom}), we acquired multiple measurements over a range of distances. The measurements were conducted after sunset to minimize the noise from the Sun for consistent results. The selection criteria for test locations were based on (1) ability to achieve direct line-of-sight between telescope and LED payload, (2) minimal light pollution to the LED payload, and (3) personal safety. While direct line-of-sight is achievable if the LED payload or telescope is located at high ground, such as at Fort Ord National Monument or Jacks Peak Park in Monterey, CA, the challenge and danger with tracking in darkness makes such locations less appealing. Another potential test location explored used the public roads around the farms at Salinas, CA. The slopes along the roads, however, prevented any direct line-of-sight between the telescope and LED payload over the intended measurement distance. In addition, there were cars accessing the road making this option less ideal. The coastal area was selected as there were sand dunes that segregate light pollution from the residential housing and freeway away from the LED payload, and the beaches are located within walking distance from the street parking. The telescope was set up at the edge of the jetty at Fisherman's Wharf while the LED payload was positioned at four different test locations along the coast as listed in Table 5. Figure 22 provides a graphical view of the test setup.

Table 5. Test locations and distance apart.

Telescope Location	LED Payload Location	Distance between Telescope and LED Payload
Fisherman's Wharf (36°36'12.9"N, 121°53'21.5"W)	Del Monte Beach (36°36'17.0"N, 121°52'10.0"W)	1.1 Miles (1.8 Km)
	Monterey State Beach (36°36'44.6"N, 121°51'29.0"W)	1.85 Miles (3.0 Km)
	Sand City Beach (36°37'06"N, 121°51'01"W)	2.4 Miles (3.9 Km)
	Moss Landing State Beach (36°48'12"N, 121°47'18"W)	19.2 Miles (24.1 Km)

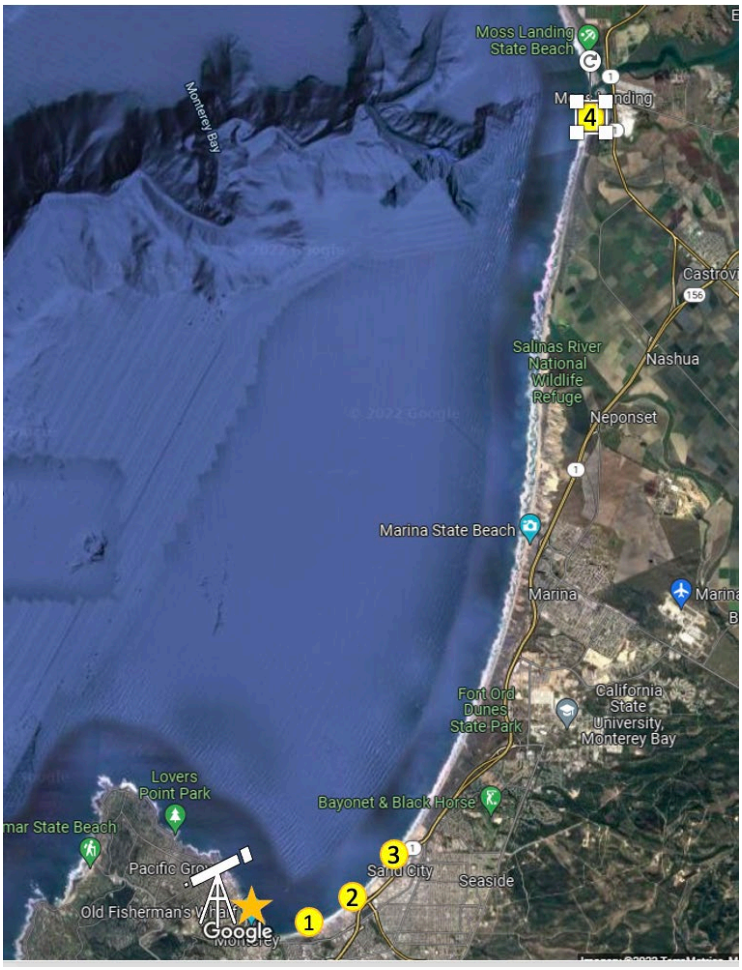

Figure 22. Locations of telescope and four identified test sites

THIS PAGE INTENTIONALLY LEFT BLANK

IV. RESULTS AND ANALYSIS

This chapter first discusses the results obtained from the link budget measurement by comparing the calculated link budget and the measurement with the MEADE LX200GPS telescope. Secondly, this chapter describes the message encoding of the LED payload and decoding from the photodiodes, which behaves as the ground station.

A. LINK BUDGET MEASUREMENT AND VERIFICATION

Based on Equation (3) in Chapter II, we observe that the atmospheric extinction loss varies as the visibility changes with the weather. In addition, the total amount of light energy collected by the receiver is dependent on the aperture size of both the transmitter and the receiver. This was evidenced during outdoor measurements where it was affected by the fog along the coastal area.

1. Link Budget Calculation

Atmospheric Extinction Loss and Geometric Loss. The visibility conditions of the Monterey Regional Airport (MRY) [38] were recorded during each test date that will be used to compare the mathematical calculation of the link budget against the measurements. Across the three test dates, the visibility varied from 1.6 miles (2.6 km) to 6.2 miles (10 km) and the visibility declined drastically after dusk as the fog built up. Using the atmospheric extinction loss (L_e) described in Equation (3) for terrestrial free-space communication, the atmospheric extinction loss could vary substantially as the distance increased. Using the highest visibility of 6.2 miles or 10 km, it would set the lowest boundary for the atmospheric extinction loss. Table 6 provides a simple comparison of the two visibility conditions from one to 20 kilometers. It is evident that the visibility conditions have an exponential impact on the atmospheric extinction loss.

The geometric loss (L_{Geom}) described in Equation (5) was calculated between the 7-inch (178 mm) MEADE LX200GPS telescope and the Cree LED (radius of 3.45 mm). The divergence angle of the Cree LED beam is 130 degrees (2268 mrad). Table 7 summarizes the total theoretical loss experienced at each test location. Geometric loss is a

function of the receiver and transmitter aperture diameter and the beam divergence angle, which does not change in different weather conditions. It was observed that the atmospheric extinction loss would vary substantially under different visibility conditions, which is primarily influenced by different weather conditions. Thus, good weather conditions play an important role in achieving a space-to-ground optical link between the LED communication payload and the receiver at the ground stations.

Table 6. Theoretical atmospheric extinction loss for different visibility conditions.

Distance (km)	**Atmospheric Extinction Loss @ Visibility = 2.6 km (dB)**	**Atmospheric Extinction Loss @ Visibility = 10 km (dB)**
1.0	8.8	1.8
5.0	44.0	8.9
10.0	88.0	17.8
15.0	132.9	26.7
20.0	175.9	35.6

Table 7. Theoretical atmospheric extinction and geometric loss at each test location.

LED Payload Location	**Distance between Telescope and LED Payload**	**Atmospheric Extinction Loss @ Visibility = 10 km (dB)**	**Geometric Loss (dB)**	**Total Loss (dB)**
Del Monte Beach (36°36’17.0”N, 121°52’10.0”W)	1.8 km	3.2	111.2	114.4
Monterey State Beach (36°36’44.6”N, 121°51’29.0”W)	3.0 km	5.3	115.7	121.0
Sand City Beach (36°37’06”N, 121°51’01”W)	3.9 km	6.9	117.9	124.9
Moss Landing State Beach (36°48’12”N, 121°47’18”W)	24.1 km	42.8	133.7	176.5

2. Transmitted Power of Cree LED

The Newport optical power meter (Model 1830C) and Newport 818-ST silicon photodetector provided by the NPS Department of Physics were used for the LED's transmission power measurement. As every component will have internal tolerance to the performance, every LED will exhibit slight differences in the brightness across its forward voltage. In our case, the LED is fixed at approximately 10 cm from the Newport 818-ST silicon photodetector as shown in Figure 23 The transmission power across different voltage levels was recorded for three different LEDs and averaged to remove any outliers in the LED performance. Figure 24 is the plot of the measurements gathered from the three different LEDs, and their performance was observed to be fairly consistent. It was observed that the increase in transmission power was marginal after 3.6 V, and the LED's temperature increased after the voltage settings were above 4.0 V.

The specifications published in the Cree LED data sheet indicates that the recommended current and forward voltage are 0.35 A and 3.3 V, which translates to 1.2 W or 0.6 dB of transmission power. However, the average measured power of -27.5 dB at 3.3V was significantly different from the theoretical value. The difference in result could potentially be due to (1) instrumental tolerance of the LED and the Newport 818-ST silicon photodetector, and (2) geometric loss as the LED has a wide viewing angle of 130 degrees. Thus, the measured transmission power would be used for the link budget calculations in place of the theoretical values. See Appendix A for detailed power measurements.

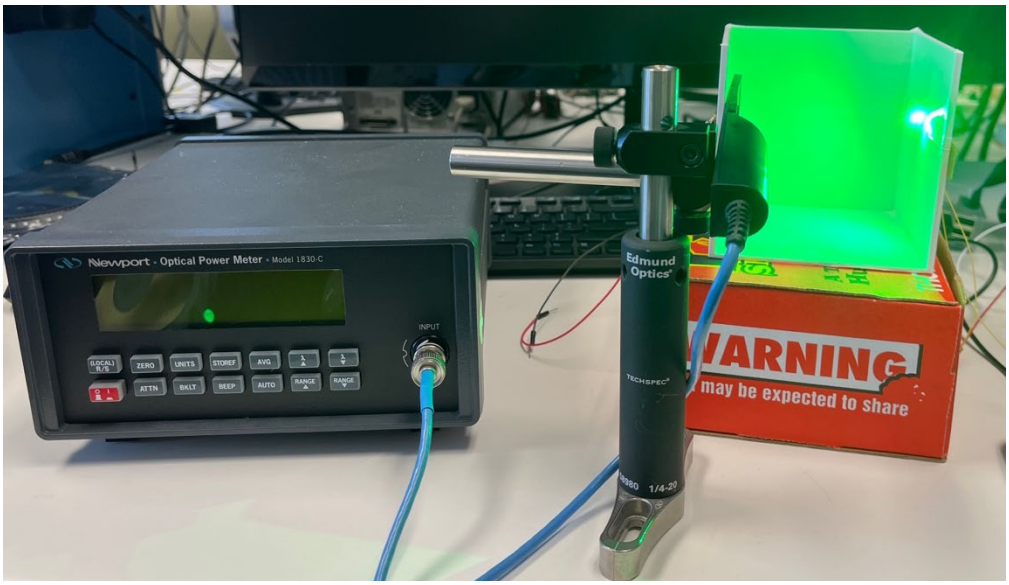

Figure 23. Cree LED transmission power measurement setup

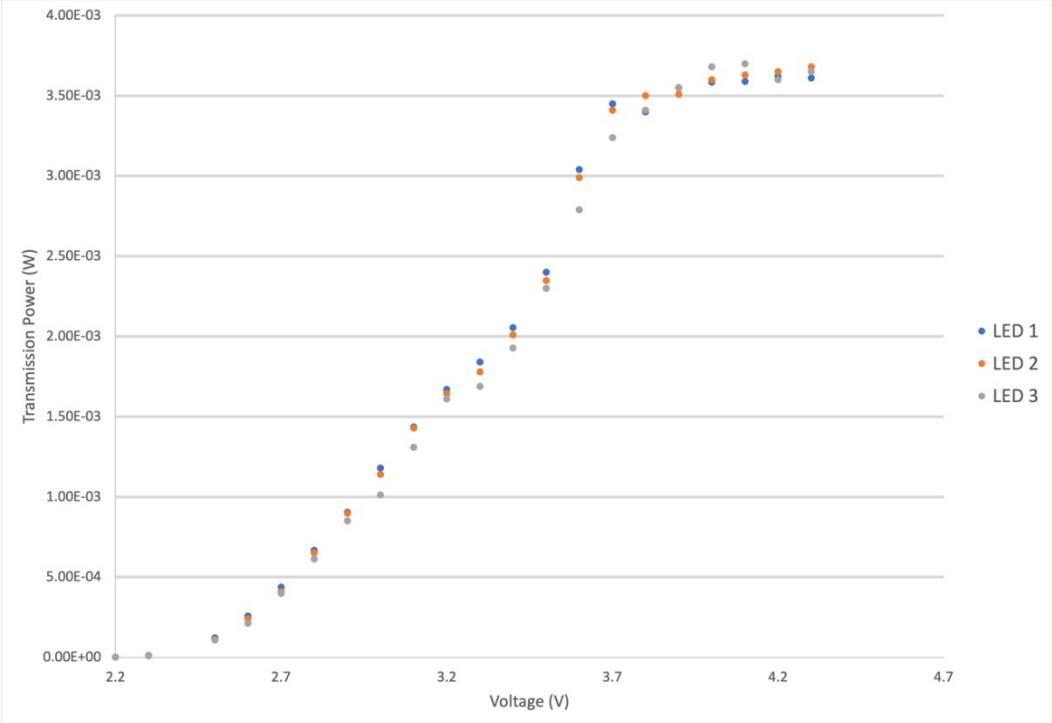

Figure 24. Transmission power measurement of three different LEDs

3. Computed Received Power

There is no active amplification used for this thesis work, and the receiver gain can be calculated based on the diameter of the receiver optical lens and the wavelength of interest Equation (9).

$$G_R = 20\,log(\frac{\pi D_R}{\lambda}) \quad (9)$$

Using the atmospheric extinction loss and geometric calculation and the LED's transmission power measurements from the earlier section, we can calculate the theoretical received power across the different test locations. The calculated received power from each test location is summarized in Table 8, based on the LED's forward voltage of 3.3 V, and Figure 25 is a graphical representation of the calculated received power at different test locations across the entire voltage range from 2.2 V to 4.3 V. It can be observed that the received power would increase significantly after the forward voltage of 3.3 V. The received power at Moss Landing is expected to be much lower as it is the furthest away from the other test locations to the telescope.

Table 8. Received power by telescope by each test location.

LED Payload Location	Measured Transmitted Power @ 3.3V (dB)	Calculated Total Loss (dB)	Calculated Receiver Gain (dB)	Calculated Received Power (dB)
Del Monte Beach (36°36'17.0"N, 121°52'10.0"W)	-24.6	-114.4	120.5	-18.6
Monterey State Beach (36°36'44.6"N, 121°51'29.0"W)	-24.6	-121.0	120.5	-25.2
Sand City Beach (36°37'06"N, 121°51'01"W)	-24.6	-124.9	120.5	-29.1
Moss Landing State Beach (36°48'12"N, 121°47'18"W)	-24.6	-176.5	120.5	-80.7

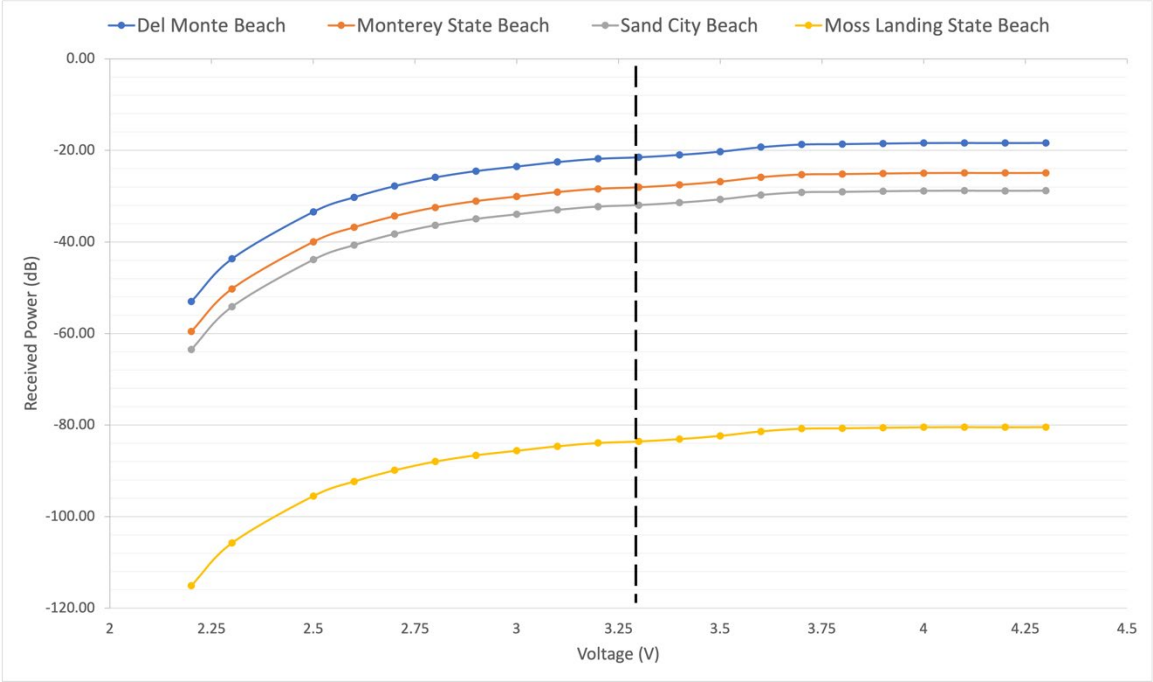

Figure 25. Calculated received power at different test locations

4. Measured Data

The measurements were carried out over three evenings as each test location and required approximately one hour each session, from setup to taking the measurement and moving to the next location. Extra time was required to search for the LED payload after setup was completed. No reading was taken at Moss Landing State Beach on all three occasions as the visibility was extremely low and the team was unable to locate the LED payload.The Canon Rebel Ti3 camera attached to the MEADE LX200GPS telescope measured and displayed the intensity of the LED payload across different voltage levels. Figure 26 is a screen capture from the digital camera at one of the test locations. Figure 27 is the graphical plot of the light intensity measured by the camera. See Appendix B for detailed measurements.

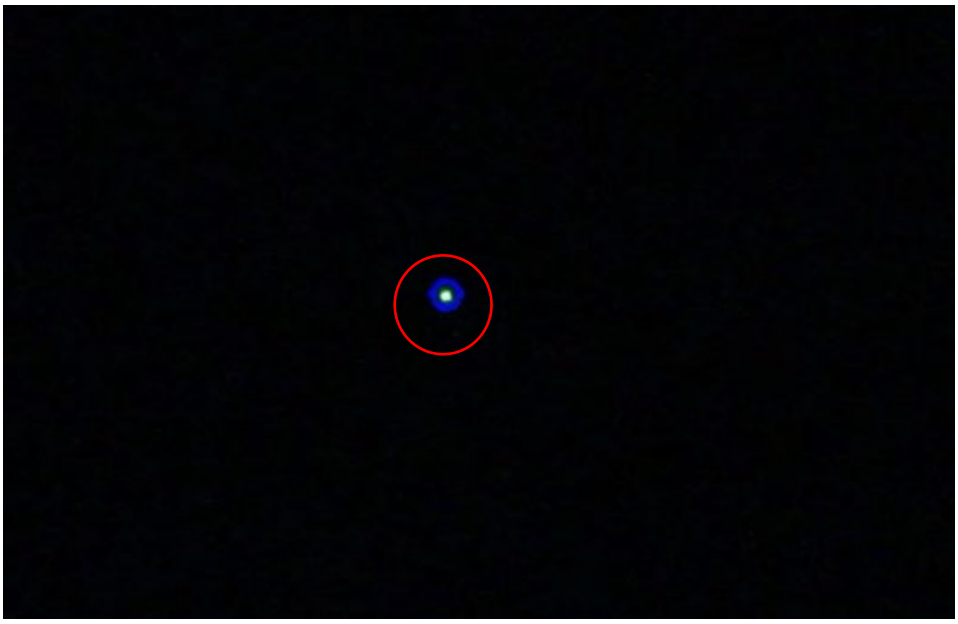

Figure 26. Screen capture of LED payload

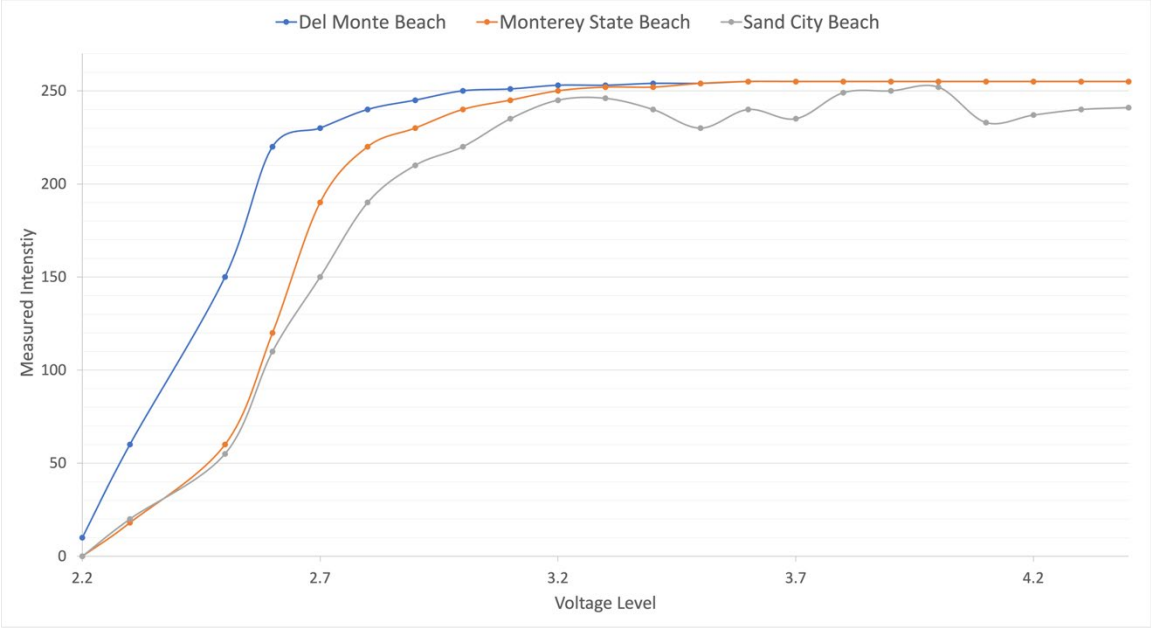

Figure 27. Intensity reading across different voltage levels at the respective test locations

5. Observation and Analysis

While the actual measurements (pixel intensity) are not in the same units as per calculation (dB), the measured data are a representation of the brightness of the LED at different voltage levels across the final three test locations. Figure 28 is the combination of the measured data plotted along the primary y-axis (dotted line) and calculated received power along the secondary y-axis at the different test locations. It is observed that both calculated and measured data reached the saturation intensity at about 3.7 V. This is consistent with the LED's performance where the recommended maximum forward voltage is 3.8 V.

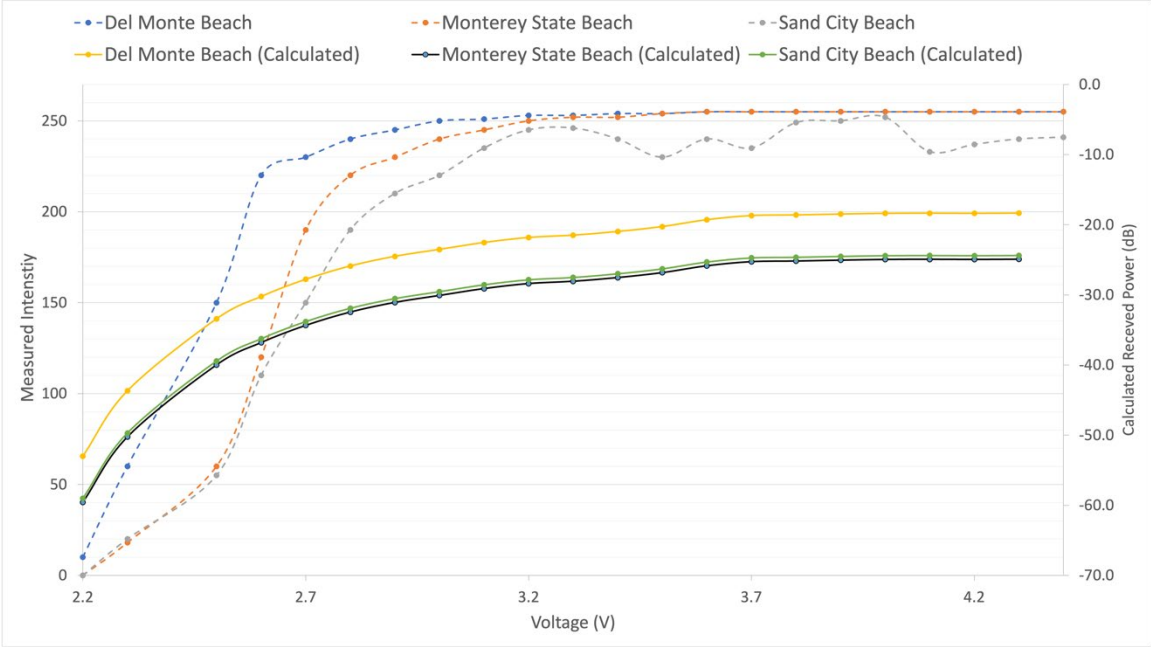

Figure 28. Calculated and measured received power across three different test locations

- The inability to capture the LED payload at Moss Landing could potentially be due to the Earth's curvature as the telescope and LED payload were both set up at the beach with no elevation. Equation (10) describes the maximum line-of-sight range that can be achieved between the receiver or the transmitter, based on the receiver height, h_r. In the test setup, the maximum

line-of-sight with the telescope height measured at 4.6 ft is approximately 2.63 NM or 4.87 km. Therefore, it will not be possible for the telescope to have visual sight on the LED payload at Moss Landing as the distance between the telescope and the payload is more than 4.87 km.

$$Range_{max}(NM) = 1.23\sqrt{h_r\,(ft)} \qquad (10)$$

- Based on the lowest reading at Del Monte Beach and the losses at this distance, the lowest power at which the telescope is capable of receiving is -53.01dBW, as depicted in Table 9. As discussed in Chapter 2, the atmospheric extinction loss is calculated up to 100 km because the atmospheric density beyond the Kármán line will be insignificant with absorption and scattering effects. Thus, it can be concluded that the LED payload will require a minimum of five LEDs operating at 3.3 V in order to achieve a positive link between the telescope and the LED payload from a LEO orbit (Table 10).

Table 9. Minimum received power of telescope.

Transmission Power @2.2V (dBW)	**Total Loss @ 1.8km apart (dB)**	**Receiver Gain**	**Minimal Received Power (dBW)**
-59.0	114.4	120.5	-53.0

Table 10. Minimum number of LEDs required at 500 km altitude.

Minimal Received Power (dBW)	**Geometric Loss @ 500km apart (dB)**	**Extinction Loss up to 100 km (dB)**	**Receiver Gain**	**Minimal number of LED required**
-53.0	160.1	36.0	120.5	(-128.6 / -27.5) > **5 LEDs**

B. MESSAGE ENCODING / DECODING AND DATA RATE VERIFICATION

The LED communication payload was designed to communicate with the Corvus-6 bus with the Universal Asynchronous Receiver/Transmitter (UART) communication protocol. In consideration that direct line of sight is required for the LED to send data to the ground stations and the LED communication payload would function as secondary or backup communication system, only the CubeSat's mode of operation and operating temperature would be sent. The software development and testing were divided into two approaches, the first without the UART communication protocol and the second using the UART communication protocol.

1. Non-UART Communication Method

In this method, each letter or digit of the message is converted from the ASCII format into eight binary bits. Subsequentially, the binary bits will be transmitted with the Raspberry Pi General-Purpose Input Output (GPIO) ports to drive the LED driver and LED (i.e., on or off representing "1" and "0"). A second Raspberry Pi will read the eight binary bits transmitted from the LED and decode the eight binary bit string into ASCII characters. Figure 29 shows the bench testing setup with the LED payload on the left side and the photodiode circuit on the right controlled by two separate Raspberry Pis. Figure 30 and Figure 31 are screen captures of the eight binary bits sent through the LED payload and the message decoded by the photodiode. This implementation was able to achieve a minimum of 1 bit per second (1 bps) sent between the LED and the photodiode. The decoding became unstable as the bit rate increased to 10 bps. The low data rate is beneficial for visual tracking and decoding of the messages manually, which functions as a backup communication system.

It was assessed that this setup was unable to achieve a higher data rate as there is inherent tolerances and delays with the internal clocks between the two Raspberry Pis and the number of executable lines of code between the encoding and decoding software is different. Thus, the time synchronization between both the LED and the photodiode would be more difficult as the bit rate increases. One possible improvement for future work is to

have an LED of a different color for time synchronization after each eight binary data bits are sent. Another future improvement is to incorporate LEDs of different wavelengths or colors, which will only light up after each set of eight bits is received before the next of eight binary bits can be transmitted.

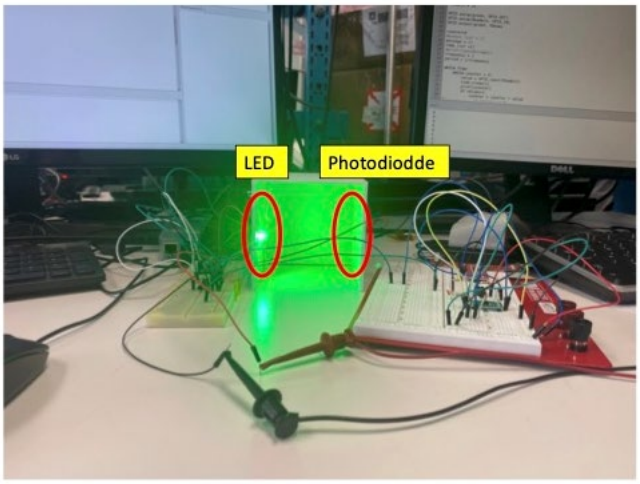

Figure 29. Bench setup of LED and photodiode circuit for data transfer

```
Python 3.9.2 (/usr/bin/python3)
>>> %Run '4. Send_Temp_LED Driver_25 Aug.py'

  56
  b'5'
  ['0', '0', '1', '1', '0', '1', '0', '1']
  b'6'
  ['0', '0', '1', '1', '0', '1', '1', '0']
  55
  b'5'
  ['0', '0', '1', '1', '0', '1', '0', '1']
  b'5'
  ['0', '0', '1', '1', '0', '1', '0', '1']
  55
  b'5'
  ['0', '0', '1', '1', '0', '1', '0', '1']
```

Figure 30. Screen capture of message sent by LED payload

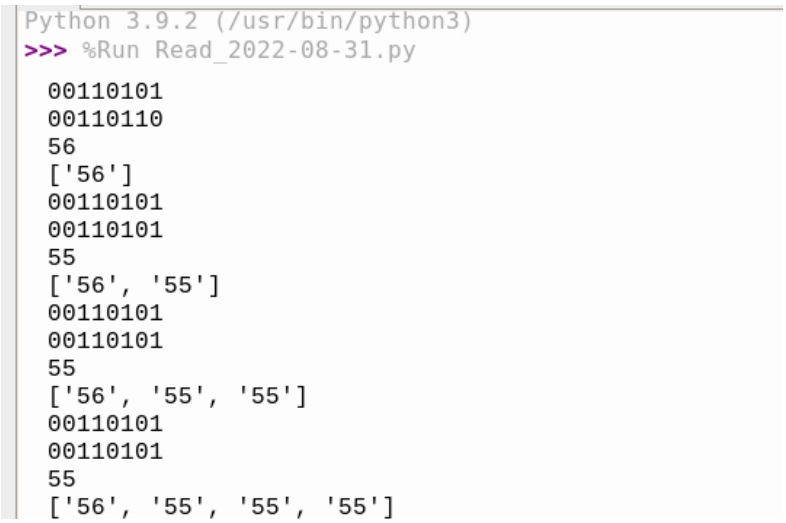

Figure 31. Screen capture of message decoded by through the photodiode

2. UART Communication Method

In this implementation, the hardware setup was identical to the previous one, except this one used the UART protocol for communication.

Both the Corvus-6 bus and the Raspberry Pi were able to communicate through the UART interface, which simplifies the exchange of messages or data between different sub-systems and the LED payload. In this implementation, the messages were sent through the LED using the UART communication protocol. The oscilloscope was able to capture the eight binary bits sent through the LED payload as shown in Figure 32. However, the photodiode could only read "high" throughput. It was assessed that the baud rate of 9,600 bps is too fast for the photodiode to respond. Hence, COTS products such as the Hyperion Technologies GD200 [39, p. 200] and the Si Avalanche Photodetectors APD210 [40], which are capable of achieving data rates up to 1 Gbps, could be explored for future development.

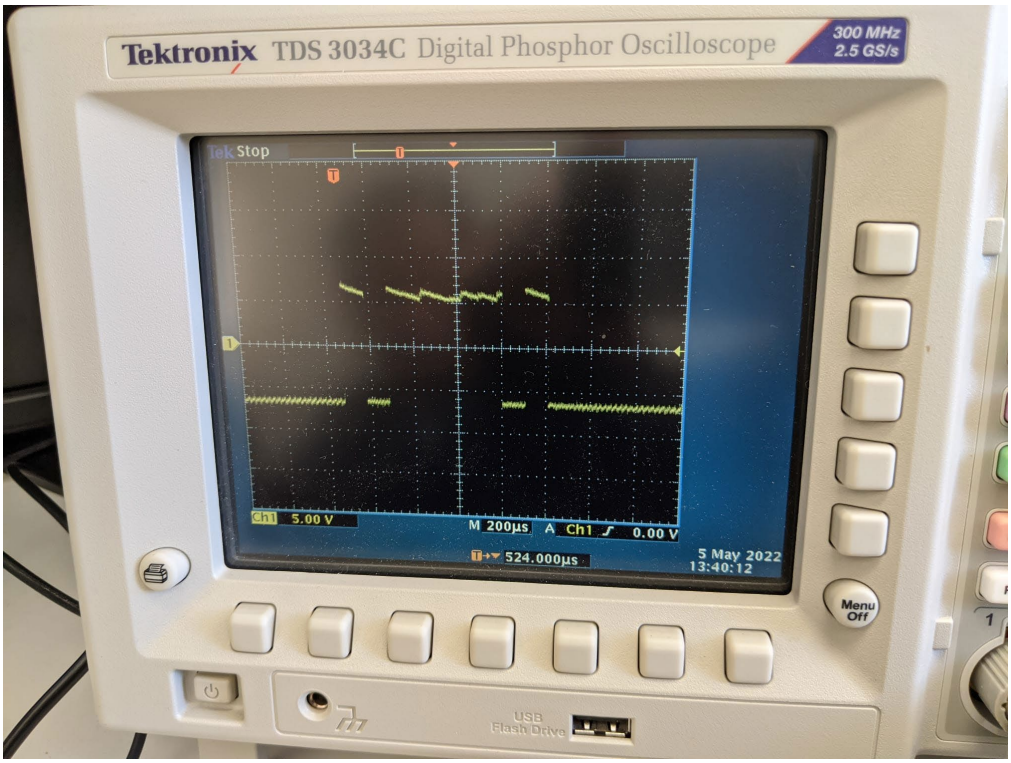

Figure 32. Oscilloscope capture of message sent through the LED payload

THIS PAGE INTENTIONALLY LEFT BLANK

V. CONCLUSION AND RECOMMENDATION

A. CONCLUSION

The SSAG at NPS has had a series of projects related to optical free-space communication over the past years. The main objectives of these studies have been to improve CubeSat tracking by providing an alternate means to the RF method and provide an alternate communication system with light waves. This thesis research sought to test and verify a viable LED communication payload to achieve optical tracking of a CubeSat in LEO, capable of transmitting a CubeSat's operating status or a warning message. In order to establish any optical communication, it is crucial to validate the link budget analysis, and so, this research put significant effort into this area. The link budget analysis accomplished in this study validated the theoretical model of the optical link budget discussed in Chapter II. The effect of weather on the measurement was also shown to be significant as the separation distance between the telescope and LED payload increased. Thus, fog build-up at dusk may potentially pose some issues with optical tracking.

The intermittent foggy weather at the Monterey, CA region may pose a challenge for attaining a constant link between the LED payload onboard the CubeSats and the ground station. This could be mitigated if the telescope is located farther inland or at a higher altitude, and one possible location could be in Carmel Valley or at Jacks Peak where there may be sufficient elevation to avoid fog cover. The other alternative is to increase the transmission power or receiver gain to cater sufficient link margin to overcome the weather condition. On this note, a location in the U.S. southwest region, where it is not affected by fog, would be a more ideal location to operate the telescope. Unfortunately, the data communication was not achieved as set in the thesis objective of utilizing UART to send messages between the LED payload and the photodiode. While we were only able to achieve a data rate of 10 bps, we were able to learn valuable lessons from this research about how future research should explore COTS products and incorporate a closed loop system to reduce the error.

B. RECOMMENDATIONS FOR FUTURE WORK

The following areas are recommended for future research and thesis work in the field of optical free-space communication and optical tracking for CubeSats.

1. Operating Wavelength

The green colored LED was chosen for this thesis work as it provides good transmittivity in our atmosphere and readily enables performing link budget analysis with visible light. Therefore, future research works can explore LEDs operating at the Near Infrared (NIR) region at about 850 nm. The amount of atmospheric extinction loss at 500 km altitude will decrease significantly from 180.2 dB to 84.6 dB by increasing the operating wavelength from 530 nm to 850 nm. In turn, less power from the CubeSat is needed to achieve the link budget between the CubeSat and ground station. To enable visual sighting of the LED for bench testing, a customized IR filter can be purchased and attached to the Canon Rebel Ti3 camera in SSAG, which costs approximately $300 [41].

2. Pulse Width Modulation

This thesis discussed the effect of weather on optical link budgets, and this was experienced during one of the outdoor measurements when the LED payload was situated at Sand City Beach. Thus, it would be reasonable to integrate extra LEDs on the CubeSat for redundancy when any LED is blown out or when there are some clouds in the sky that will attenuate the light signal. This would result in higher power consumption from the CubeSat battery, which could affect other system operations during eclipse passes. It is recommended, therefore, that future research work consider Pulse Width Modulation (PWM) or other modulation methods. The LED's brightness intensity can be adjusted by altering the duty cycle and adjusting the amount of power consumption from the payload correspondingly.

3. Ground Station Implementation

This thesis was unable to achieve free-space communication between the LED and the photodiode circuit. Future research can focus on verifying the encoding and decoding of messages between the CubeSat and ground station by using a COTS product such as the

Hyperion Technologies GD200 and the Si Avalanche Photodetectors APD210, which can achieve data rates up to 1 Gbps. The detector will convert light or laser beams into digital bitstreams ready for message processing at the ground station. Each detector costs upwards of $2,000.

4. Future Software Improvement

The current design of the communication method between the LED communication payload and the photodiode is an open-loop system in which there is no feedback between the sender (LED payload) and the receiver (photodiode). Both the sender and the receiver are operating on their respective internal clocks, and they can drift over time. One improvement is to incorporate an LED operating on a different wavelength (e.g., red color in the 620 nm range) and have the ground station use a separate photodiode to monitor the red LED as a start or stop bit. This should reduce the error rate encountered in the current setup.

THIS PAGE INTENTIONALLY LEFT BLANK

APPENDIX A. POWER MEASUREMENT OF LEDS

Voltage level	LED 1 (W)	LED 2 (W)	LED 3 (W)	Average Power (W)	Average Power (dB)
2.2	1.26×10^{-6}	1.29×10^{-6}	1.19×10^{-6}	1.25×10^{-6}	-59.04
2.3	1.06×10^{-5}	1.16×10^{-5}	0.99×10^{-5}	1.07×10^{-5}	-49.71
2.5	1.12×10^{-4}	1.21×10^{-4}	1.08×10^{-4}	1.14×10^{-4}	-39.44
2.6	2.40×10^{-4}	2.57×10^{-4}	2.10×10^{-4}	2.36×10^{-4}	-36.23
2.7	4.10×10^{-4}	4.38×10^{-4}	3.99×10^{-4}	4.16×10^{-4}	-33.81
2.8	6.51×10^{-4}	6.68×10^{-4}	6.13×10^{-4}	6.44×10^{-4}	-31.91
2.9	8.97×10^{-4}	9.05×10^{-4}	8.50×10^{-4}	8.84×10^{-4}	-30.54
3.0	1.14×10^{-3}	1.18×10^{-3}	1.01×10^{-3}	1.11×10^{-3}	-29.54
3.1	1.43×10^{-3}	1.44×10^{-3}	1.31×10^{-3}	1.39×10^{-3}	-28.56
3.2	1.64×10^{-3}	1.67×10^{-3}	1.61×10^{-3}	1.64×10^{-3}	-27.85
3.3	1.78×10^{-3}	1.84×10^{-3}	1.69×10^{-3}	1.77×10^{-3}	-27.52
3.4	2.01×10^{-3}	2.06×10^{-3}	1.93×10^{-3}	2.00×10^{-3}	-26.99
3.5	2.53×10^{-3}	2.40×10^{-3}	2.30×10^{-3}	2.35×10^{-3}	-26.29
3.6	2.99×10^{-3}	3.04×10^{-3}	2.79×10^{-3}	2.94×10^{-3}	-25.32
3.7	3.45×10^{-3}	3.41×10^{-3}	3.24×10^{-3}	3.37×10^{-3}	-24.73
3.8	3.40×10^{-3}	3.50×10^{-3}	3.41×10^{-3}	3.44×10^{-3}	-24.64
3.9	3.55×10^{-3}	3.51×10^{-3}	3.55×10^{-3}	3.54×10^{-3}	-24.51
4.0	3.58×10^{-3}	3.60×10^{-3}	3.68×10^{-3}	3.62×10^{-3}	-24.41
4.1	3.59×10^{-3}	3.63×10^{-3}	3.70×10^{-3}	3.64×10^{-3}	-24.39
4.2	3.62×10^{-3}	3.65×10^{-3}	3.60×10^{-3}	3.62×10^{-3}	-24.41
4.3	3.61×10^{-3}	3.68×10^{-3}	3.65×10^{-3}	3.65×10^{-3}	-24.38

THIS PAGE INTENTIONALLY LEFT BLANK

APPENDIX B. INTENSITY MEASUREMENTS FROM CAMERA

Voltage	Del Monte Beach	Monterey State Beach	Sand City Beach
2.2	10	0	0
2.3	60	18	20
2.5	150	60	55
2.6	220	120	110
2.7	230	190	150
2.8	240	220	190
2.9	245	230	210
3.0	250	240	220
3.1	251	245	235
3.2	253	250	245
3.3	253	252	246
3.4	254	252	240
3.5	254	254	230
3.6	255	255	240
3.7	255	255	235
3.8	255	255	249
3.9	255	255	250
4.0	255	255	252
4.1	255	255	233
4.2	255	255	237
4.3	255	255	240

THIS PAGE INTENTIONALLY LEFT BLANK

LIST OF REFERENCES

[1] Statista. “Number of active satellites by year 1957–2021.” Accessed Jul. 14, 2022. [Online], Available: https://www.statista.com/statistics/897719/number-of-active-satellites-by-year/.

[2] European Space Agency, “Swarm reveals why satellites lose track.” Accessed Aug. 13, 2022, [Online], Available: https://www.esa.int/Applications/Observing_the_Earth/FutureEO/Swarm/Swarm_reveals_why_satellites_lose_track.

[3] E. Kulu, “Nanosats Database,” 2022 [Online]. Available: https://www.nanosats.eu/index.html.

[4] Statista, “Infographic: The Countries with the Most Satellites in Space,” Accessed Jul. 14, 2022. [Online], Available: https://www.statista.com/chart/17107/countries-with-the-most-satellites-in-space/.

[5] S. Loff, “CubeSats Overview,” *NASA*, Jul. 22, 2015. [Online], Available: http://www.nasa.gov/mission_pages/cubesats/overview.

[6] GISGeography, “The CubeSat: Small Satellites for Big Ideas,” Apr. 22, 2022. [Online], Available: https://gisgeography.com/cubesat/.

[7] Elizabeth. Howell, “CubeSats: Tiny Payloads, Huge Benefits for Space Research,” *Space.com*, Jun. 19, 2018. [Online]. Available: https://www.space.com/34324-cubesats.html.

[8] Elizabeth Howell, “NASA’s 1st Artemis moon landing will likely slip another year to 2026 | Space,” Mar 01, 2022. [Online], Available: https://www.space.com/artemis-moon-landing-likely-slip-to-2026.

[9] A. Cook, “Psyche Mission FAQ | Psyche Mission - A Mission to a Metal World,” *Psyche Mission*. Accessed Jul.10 2022. [Online], Available: https://psyche.asu.edu/mission/faq/.

[10] C. Cuiule, “Cost Drivers of CubeSats,” *PRICE Systems*, May 19, 2020. [Online], Available: https://www.pricesystems.com/cost-drivers-of-cubesats/.

[11] A. K. Nervold, J. Berk, J. Straub, and D. Whalen, “A Pathway to Small Satellite Market Growth,” *Advances in Aerospace Science and Technology*, vol. 01, no. 01, Art. no. 01, 2016.

[12] Alen. Space, “10 Advantages of CubeSats vs. Conventional Satellites.” Accessed Jul. 10, 2022. [Online], Available: https://info.alen.space/advantages-of-cubesats-vs-conventional-satellites.

[13] Jennifer Harbaugh, “Secondary Payloads – Artemis,” blog, Oct 4, 2021 [Online]. Available: https://blog.nasa.gov/artemis/tag/secondary-payloads/

[14] H. W. Jones, “The Recent Large Reduction in Space Launch Cost,” p. 10.

[15] P. Marzioli *et al.*, “Usage of Light Emitting Diodes (LEDs) for improved satellite tracking,” *Acta Astronautica*, vol. 179, pp. 228–237, Feb. 2021, doi: 10.1016/j.actaastro.2020.10.023.

[16] ScienceDirect Topics, “Space Surveillance - an overview.” Accessed Jul. 10, 2022. [Online], Available: https://www.sciencedirect.com/topics/engineering/space-surveillance.

[17] NASA. “12.0 Identification and Tracking Systems | NASA.” Accessed Jul. 10, 2022. [Online], Available: https://www.nasa.gov/smallsat-institute/sst-soa/identification-and-tracking-systems.

[18] Aerospace America. “Tracking cubesats,” May 01, 2020. [Online], Available: https://aerospaceamerica.aiaa.org/departments/tracking-cubesats/.

[19] A. Novak, A. Schuett, A. Parker, “The Rise of Cubesats: Opportunities and Challenges,” blog, Feb 7, 2022 [Online]. Available: https://www.wilsoncenter.org/blog-post/rise-cubesats-opportunities-and-challenges.

[20] European Space Agency, “ESA Science & Technology - Blackbody radiation.” Accessed Jul. 17, 2022. [Online], Available: https://sci.esa.int/web/education/-/48986-blackbody-radiation.

[21] Science Mission Directorate. “Introduction to the Electromagnetic Spectrum.” Accessed Jul. 17, 2022. [Online], Available: https://science.nasa.gov/ems/01_intro.

[22] IET Digital Library. “*Principles and Applications of Free Space Optical Communications*..” 2019. doi: 10.1049/PBTE078E.

[23] J. L. Green, B. W. Welch, and R. M. Manning, “Optical Communication Link Atmospheric Attenuation Model,” E-19597, Feb. 2019. [Online]. Available: https://ntrs.nasa.gov/citations/20190001012

[24] Research Gate. “Figure 1. Atmospheric absorption across the electromagnetic spectrum..” Accessed Jul. 19, 2022. [Online], Available: https://www.researchgate.net/figure/Atmospheric-absorption-across-the-electromagnetic-spectrum-High-energy-waves-past-the_fig1_282270380.

[25] E. Leitgeb, M. Gebhart, and U. Birnbacher, “Optical networks, last mile access and applications,” *Journal of Optical and Fiber Communications Reports*, vol. 2, pp. 56–85, Mar. 2005, doi: 10.1007/s10297-004-0025-x.

[26] A. Berk, P. Conforti, and F. Hawes, “An accelerated line-by-line option for MODTRAN combining on-the-fly generation of line center absorption within 0.1 cm-1 bins and pre-computed line tails,” Baltimore, Maryland, United States, May 2015, p. 947217. doi: 10.1117/12.2177444.

[27] S. Dasso, A. Gulisano, J. Masías-Meza, and H. Asorey, “A Project to Install Water-Cherenkov Detectors in the Antarctic Peninsula as part of the LAGO Detection Network,” Aug. 2016, p. 105. doi: 10.22323/1.236.0105.

[28] BYJUS. “Visible Light - The Electromagnetic Spectrum Color.” Accessed Jul. 19, 2022. [Online], Available: https://byjus.com/physics/visible-light/.

[29] Spectral Sciences Inc. “MODTRAN®.” Accessed Jul. 19, 2022. [Online], Available: http://modtran.spectral.com/modtran_home#plot.

[30] James R. Wertz, and Wiley J. Larson, “Space mission engineering: the new SMAD,” 2011, pp 649 - 652

[31] C. Haughwout, “Non-coherent LED Arrays as Ground Beacons for Small Satellite Optical Communications Systems,” 2018, p. 8.

[32] Wavelength Electronics. “PHOTODIODE BASICS.” Accessed Jul. 22, 2022. [Online], Available: https://www.teamwavelength.com/photodiode-basics/.

[33] Electronics Notes. “What is a Phototransistor.” Accessed Jul. 22, 2022. [Online], Available: https://www.electronics-notes.com/articles/electronic_components/transistor/what-is-a-phototransistor-tutorial.php.

[34] OSRAM. “OSRAM Radial T1 Ambient Light Sensor, SFH 3310 | OSRAM Opto Semiconductors.” Accessed Jul. 31, 2022. [Online], Available; https://www.osram.com/ecat/com/en/class_pim_web_catalog_103489/prd_pim_device_2219678/.

[35] North Coast Photographic Service. “Digital Explained,” Accessed Jul. 31, 2022. [Online], Available: https://northcoastphoto.com/digital-explained/.

[36] ScienceDirect Topics. “Pixel Intensity - an overview.” Accessed Jul. 31, 2022. [Online], Available: https://www-sciencedirect-com.libproxy.nps.edu/topics/computer-science/pixel-intensity.

[37] Tutorial Point. “Concept of Pixel.” Accessed Jul. 31, 2022. [Online], Available: https://www.tutorialspoint.com/dip/Concept_of_Pixel.htm.

[38] Globalair. “MONTEREY RGNL Weather - MRY Aviation Weather.” Accessed Aug. 14, 2022. [Online], Available: https://www.globalair.com/airport/apt.weather.aspx?aptcode=mry.

[39] Orbital Transports. “GD200 Gigabit Detector.” Accessed Aug. 16, 2022. [Online], Available: https://catalog.orbitaltransports.com/gd200-gigabit-detector/.

[40] Thorlab. “Si Avalanche Photodetectors.” Accessed Aug. 16, 2022. [Online], Available: https://www.thorlabs.com/newgrouppage9.cfm?objectgroup_id=6686.

[41] Kolari Vision. “Canon DSLR and Mirrorless Infrared Conversion Service.” Accessed Aug. 16, 2022. [Online], Available: https://kolarivision.com/product/canon-dslr-infrared-conversion/.

INITIAL DISTRIBUTION LIST

1. Defense Technical Information Center
   Ft. Belvoir, Virginia

2. Dudley Knox Library
   Naval Postgraduate School
   Monterey, California